Missouri University of Science and Technology
Scholars' Mine

Physics Faculty Research & Creative Works | Physics

01 Sep 2017

All-Sky Search for Periodic Gravitational Waves in the O1 LIGO Data

Benjamin P. Abbott

Marco Cavaglia
Missouri University of Science and Technology, cavagliam@mst.edu

For full list of authors, see publisher's website.

Follow this and additional works at: https://scholarsmine.mst.edu/phys_facwork

Part of the Physics Commons

Recommended Citation

B. P. Abbott et al., "All-Sky Search for Periodic Gravitational Waves in the O1 LIGO Data," *Physical Review D*, vol. 96, no. 6, American Physical Society (APS), Sep 2017.
The definitive version is available at https://doi.org/10.1103/PhysRevD.96.062002

This Article - Journal is brought to you for free and open access by Scholars' Mine. It has been accepted for inclusion in Physics Faculty Research & Creative Works by an authorized administrator of Scholars' Mine. This work is protected by U. S. Copyright Law. Unauthorized use including reproduction for redistribution requires the permission of the copyright holder. For more information, please contact scholarsmine@mst.edu.

PHYSICAL REVIEW D **96,** 062002 (2017)

All-sky search for periodic gravitational waves in the O1 LIGO data

B. P. Abbott *et al.*[*]
(LIGO Scientific Collaboration and Virgo Collaboration)
(Received 10 July 2017; published 12 September 2017)

We report on an all-sky search for periodic gravitational waves in the frequency band 20–475 Hz and with a frequency time derivative in the range of $[-1.0, +0.1] \times 10^{-8}$ Hz/s. Such a signal could be produced by a nearby spinning and slightly nonaxisymmetric isolated neutron star in our galaxy. This search uses the data from Advanced LIGO's first observational run, O1. No periodic gravitational wave signals were observed, and upper limits were placed on their strengths. The lowest upper limits on worst-case (linearly polarized) strain amplitude h_0 are $\sim 4 \times 10^{-25}$ near 170 Hz. For a circularly polarized source (most favorable orientation), the smallest upper limits obtained are $\sim 1.5 \times 10^{-25}$. These upper limits refer to all sky locations and the entire range of frequency derivative values. For a population-averaged ensemble of sky locations and stellar orientations, the lowest upper limits obtained for the strain amplitude are $\sim 2.5 \times 10^{-25}$.

DOI: 10.1103/PhysRevD.96.062002

I. INTRODUCTION

We report the results of an all-sky, multipipeline search for continuous, nearly monochromatic gravitational waves from rapidly rotating isolated neutron stars using data from the first observing run (O1) of the Advanced Laser Interferometer Gravitational wave Observatory (Advanced LIGO [1]). Several different analysis algorithms are employed and cover frequencies from 20 Hz through 475 Hz and frequency derivatives over the range $[-1.0, +0.1] \times 10^{-8}$ s.

A number of previous searches for periodic gravitational waves from isolated neutron stars have been carried out in initial LIGO and Virgo data [2–23]. These searches have included coherent searches for gravitational radiation from known radio and X-ray pulsars, directed searches for known stars or locations having unknown signal frequencies, and spotlight or all-sky searches for stars with unknown signal frequency and sky location.

Here, we apply four different all-sky search programs (pipelines) used in previous searches. In summary,

(a) The *PowerFlux* pipeline has been used in previous searches of initial LIGO data from the S4, S5 and S6 Science Runs [12,14,16,20]. The program uses a *Loosely Coherent* method for following up outliers [24], and also a new universal statistic that provides correct upper limits regardless of the noise distribution of the underlying data, but which yields near-optimal performance for Gaussian data [25].

(b) The *FrequencyHough* hierarchical pipeline has been used in the previous all-sky search of Virgo VSR2 and VSR4 Science Runs [23]. It consists of an initial multistage phase, in which candidates are produced, and a follow-up phase in which the candidates are confirmed or discarded. Frequentist upper limits are computed with a computationally cheap procedure, based on the injection of a large number of simulated signals into the data.

(c) The *SkyHough* pipeline has been used in previous searches of initial LIGO data from the S2, S4 and S5 Science Runs [11,12,18], as well as in the second stage of Einstein@Home searches [13,15]. An improved pipeline applying a clustering algorithm to coincident candidates was employed in [26]. Frequentist upper limits are derived based on a number of simulated software signal injections into the data.

(d) The *Time-Domain $\mathcal{F}$-statistic* pipeline has been used in the all-sky search of the Virgo VSR1 data [19]. This program performs a coherent analysis of narrow-band time-domain sequences (each a few days long) with the $\mathcal{F}$-statistic method [27], followed by a search for coincidences among candidates found in different time sequences, for a given band. In order to estimate the sensitivity, frequentist upper limits are obtained by injecting simulated signals into the data.

These different analysis programs employ a variety of algorithmic and parameter choices in order to reduce the possibility of discarding a gravitational wave signal due to suboptimal treatment of detector artifacts or by adhering to an overly restrictive signal model. The coherence times used in first-stage data processing range from 1800 s to 6 days, and the treatment of narrow spectral artifacts ("lines") differs substantially among the different search programs. The latter is an especially important consideration for the O1 data set because lines are, unfortunately, especially prevalent.

After following up the first-stage outliers, none of the different search pipelines found evidence for continuous gravitational waves in the O1 data over the range of frequencies and frequency derivatives searched. Upper

[*]Full author list given at the end of the article.

 © 2017 American Physical Society

limits are derived for each analysis, with some variation in techniques among the different programs.

This article is organized as follows: Section II describes the Advanced LIGO interferometers and the first observing run. Section III provides an overview of the four pipelines, discussing common and differing features. The individual pipelines are described in more detail in Sec. IV. In Sec V, the results of these four searches are presented, describing both the outliers and their follow up, and the derived upper limits. Finally, we conclude in Sec. VI.

II. LIGO INTERFEROMETERS AND THE O1 OBSERVING RUN

Advanced LIGO consists of two detectors, one in Hanford, Washington, and the other in Livingston, Louisiana, separated by a ∼3000-km baseline [28]. Each site hosts one 4-km-long interferometer inside a vacuum envelope with the primary interferometer optics suspended by a cascaded, quadruple suspension system in order to isolate them from external disturbances. The interferometer mirrors act as test masses, and the passage of a gravitational wave induces a differential-arm length change which is proportional to the gravitational wave strain amplitude. The Advanced LIGO detectors began data collecting in September 2015 after a major upgrade targeting a 10-fold improvement in sensitivity over the initial LIGO detectors. While not yet operating at design sensitivity, both detectors reached an instrument noise 3 to 4 times lower than the previous best with the initial-generation detectors in their most sensitive frequency band between 100 Hz and 300 Hz [29].

Advanced LIGO's first observing run occurred between September 12, 2015 and January 19, 2016, for which approximately 77 days and 66 days of analyzable data was produced by the Hanford (H1) and Livingston (L1) interferometers, respectively. Notable instrumental contaminations affecting the searches described here included spectral combs of narrow lines in both interferometers, many of which were identified after the run ended and mitigated for future running. These artifacts included an 8-Hz comb in H1 with the even harmonics (16-Hz comb) being especially strong, which was later tracked down to digitization roundoff error in a high-frequency excitation applied to servo-control the cavity length of the Output Mode Cleaner (OMC). Similarly, a set of lines found to be linear combinations of 22.7 Hz and 25.6 Hz in the L1 data was tracked down to OMC excitation at a still higher frequency, for which digitization error occurred.

In addition, the low-frequency band of the H1 and L1 data (below ∼140 Hz) was heavily contaminated by combs with spacings of 1 Hz, near-1 Hz and 0.5 Hz and a variety of nonzero offsets from harmonicity. Many of these lines originated from the observatory timing system, which includes both GPS-locked clocks and free-running local oscillators. The couplings into the interferometer appeared to come primarily through common current draws among power supplies in electronics racks. These couplings were reduced following O1 via isolation of power supplies, and in some cases, reduction of periodic current draws in the timing system itself (blinking LEDs). A subset of these lines with common origins at the two observatories contaminated the O1 search for a stochastic background of gravitational waves, which relies upon cross correlation of H1 and L1 data, requiring excision of affected bands [30].

Although most of these strong and narrow lines are stationary in frequency and hence do not exhibit the Doppler modulations due to the Earth's motion expected for a continuous wave signal from most sky locations, the lines pollute the spectrum for such sources. In sky locations near the ecliptic poles, the lines contribute extreme contamination for certain signal frequencies. For a run like O1 that spans only a modest fraction of a full year, there are also other regions of the sky and spin-down parameter space for which the Earth's average acceleration toward the Sun largely cancels a nonzero source frequency derivative, leading to signal templates with substantial contamination from stationary instrumental lines [12]. The search programs used here have chosen a variety of methods to cope with this contamination, as described below.

III. OVERVIEW OF SEARCH PIPELINES

The four search pipelines have many features in common, but also have important differences, both major and minor. In this section we provide a broad overview of similarities and differences before describing the individual pipelines in more detail in the following section.

A. Signal model

All four search methods presented here assume the same signal model, based on a classical model of a spinning neutron star with a time-varying quadrupole moment that produces circularly polarized gravitational radiation along the rotation axis and linearly polarized radiation in the directions perpendicular to the rotation axis. The linear polarization is the most unfavorable case because the gravitational wave flux impinging on the detectors is smallest compared to the flux from circularly polarized waves.

The assumed strain signal model for a periodic source is given as

$$h(t) = h_0\Big(F_+(t,\alpha_0,\delta_0,\psi)\frac{1+\cos^2(\iota)}{2}\cos(\Phi(t)) + F_\times(t,\alpha_0,\delta_0,\psi)\cos(\iota)\sin(\Phi(t))\Big), \quad (1)$$

where F_+ and $F_\times$ characterize the detector responses to signals with "+" and "×" quadrupolar polarizations [12,14,16], the sky location is described by right ascension

α_0 and declination δ_0, ψ is the polarization angle of the projected source rotation axis in the sky plane, and the inclination of the source rotation axis to the detector line of sight is ι. The phase evolution of the signal is given by the formula

$$\Phi(t) = 2\pi(f_{\text{source}} \cdot (t - t_0) + f^{(1)} \cdot (t - t_0)^2/2) + \phi, \quad (2)$$

where f_{source} is the source frequency, $f^{(1)}$ is the first frequency derivative (which, when negative, is termed the *spin-down*), time in the Solar System barycenter is t, and the initial phase ϕ is computed relative to reference time t_0. When expressed as a function of local time of ground-based detectors, Eq. (2) acquires sky-position-dependent Doppler shift terms.

Most natural sources are expected to have a negative first frequency derivative, as the energy lost in gravitational or electromagnetic waves would make the source spin more slowly. The frequency derivative can be positive when the source is affected by a strong slowly varying Doppler shift, such as due to a long-period orbit with a companion.

B. Detection statistics

All four methods look for excess detected strain power that follows a time evolution of peak frequency consistent with the signal model. Each program begins with sets of "short Fourier transforms" (SFTs) that span the observation period, with coherence times ranging from 1800 to 7200 s. The first three pipelines (*PowerFlux*, *FrequencyHough* and *SkyHough*) compute measures of strain power directly from the SFTs and create detection statistics by stacking those powers or stacking weights for powers exceeding threshold, with corrections for frequency evolution applied in the semicoherent power stacking. The fourth pipeline (*Time-Domain $\mathcal{F}$-statistic*) uses a much longer coherence time (6 d) and applies frequency evolution corrections coherently in band-limited time-domain data recreated from the SFT sets, to obtain the $\mathcal{F}$-statistic [27]. Coincidences are then required among multiple data segments with no stacking.

The *PowerFlux* method includes explicit searches over different signal polarizations, while the other three methods use a detection statistic that performs well on average over an ensemble of polarizations.

All methods search for initial frequency in the range 20–2000 Hz, but with template grid spacings that depend inversely upon the effective coherence time used.

The range of $\dot{f}$ values searched is $[-1 \times 10^{-8}, +1 \times 10^{-9}]$ Hzs^{-1}. All known isolated pulsars spin down more slowly than the two values of $|\dot{f}|_{\text{max}}$ used here, and as seen in the results section, the ellipticity required for higher $|\dot{f}|$ is improbably high for a source losing rotational energy primarily via gravitational radiation at low frequencies. A small number of isolated pulsars in globular clusters exhibit slight spin-up, believed to arise from acceleration in the Earth's direction; such spin-up values have magnitudes small enough to be detectable with the zero-spin-down templates used in these searches, given a strong enough signal. Another potential source of apparent spin-up is Dopper modulation from an unseen, long-period binary companion.

C. Upper limits

While the parameter space searched is the same for the three methods, there are important differences in the way upper limits are determined. The *PowerFlux* pipeline sets strict frequentist upper limits on detected strain power in circular and linear polarizations that apply everywhere on the sky except for small regions near the ecliptic poles, where signals with small Doppler modulations can be masked by stationary instrumental spectral lines. The other three pipelines set population-averaged upper limits over the parameter search volume, relying upon Monte Carlo simulations.

D. Outlier follow-up

The *PowerFlux* and *FrequencyHough* pipelines have hierarchical structures that permit systematic follow-up of loud outliers in the initial stage to improve intrinsic strain sensitivity by increasing effective coherence time while dramatically reducing the parameter space volume over which the follow-up is pursued. The *PowerFlux* pipeline uses "loose coherence" [24] with stages of improving refinement via steadily increasing effective coherence times, while the *FrequencyHough* pipeline increases the effective coherence time by a factor of 10 and recomputes strain power "peakmaps." Any outliers that survive all stages of any of the four pipelines are examined manually for contamination from known instrumental artifacts and for evidence of contamination from a previously unknown single-interferometer artifact. Those for which no artifacts are found are subjected to the additional systematic follow-up used for Einstein@Home searches [31,32], which includes a final stage with full coherence across the entire data run.

IV. DETAILS OF SEARCH METHODS

A. *PowerFlux* search method

The *PowerFlux* search pipeline has two principal stages. First, the main *PowerFlux* algorithm [12,14,16,33–35] is run to establish upper limits and produce lists of outliers with signal-to-noise ratio (SNR) greater than a threshold of 5. These outliers are then followed up with the *Loosely Coherent* detection pipeline [16,24,36], which is used to reject or confirm the outliers.

Both algorithms calculate power for a bank of signal model templates. The upper limits and signal-to-noise ratios for each template are computed by comparison to

TABLE I. *PowerFlux* analysis pipeline parameters. Starting with stage 1, all stages used the *Loosely Coherent* algorithm for demodulation. The sky and frequency refinement parameters are relative to values used in the semicoherent *PowerFlux* search.

Stage	Instrument sum	Phase coherence rad	Spin-down step Hz/s	Sky refinement	Frequency refinement	SNR increase %
0	initial/upper limit semicoherent	NA	1×10^{-10}	1	1/2	NA
1	incoherent	$\pi/2$	1.0×10^{-10}	1/4	1/8	20
2	coherent	$\pi/2$	5.0×10^{-11}	1/4	1/8	10
3	coherent	$\pi/4$	2.5×10^{-11}	1/8	1/16	10
4	coherent	$\pi/8$	5.0×10^{-12}	1/16	1/32	7

templates with nearby frequencies and the same sky location and spin-down [25,33,34]. The calibrated detector output time series, $h(t)$, for each detector, is broken into 50%-overlapping 7200 s-long segments which are Hann-windowed and Fourier-transformed. The resulting short Fourier transforms are arranged into an input matrix with time and frequency dimensions. The power calculation of the data can be expressed as a bilinear form of the input matrix $\{a_{t,f}\}$,

$$P[f] = \sum_{t_1,t_2} a_{t_1,f+\Delta f(t_1)} a^*_{t_2,f+\Delta f(t_2)} K_{t_1,t_2,f}, \tag{3}$$

where $\Delta f(t)$ is the detector frame frequency drift due to the effects from both Doppler shifts and the first frequency derivative. The sum is taken over all times t corresponding to the midpoint of the short Fourier transform time interval. The kernel $K_{t_1,t_2,f}$ includes the contribution of time-dependent SFT noise weights, antenna response, signal polarization parameters and relative phase terms [24,36].

The first-stage *PowerFlux* algorithm uses a kernel with main diagonal terms only and is very fast. The second-stage *Loosely Coherent* algorithm increases coherence time while still allowing for controlled deviation in phase [24]. This is done by more complicated kernels that increase effective coherence length.

The effective coherence length is captured in a parameter δ, which describes the amount of phase drift that the kernel allows between SFTs. A value of $\delta = 0$ corresponds to a fully coherent case, and $\delta = 2\pi$ corresponds to incoherent power sums.

Depending on the terms used, the data from different interferometers can be combined incoherently (such as in stages 0 and 1, see Table I) or coherently (as used in stages 2, 3 and 4). The coherent combination is more computationally expensive but provides much better parameter estimation.

The upper limits presented in Sec. V B (Fig. 15) are reported in terms of the worst-case value of h_0 (which applies to linear polarizations with $\iota = \pi/2$) and for the most sensitive circular polarization ($\iota = 0$ or π). As described previously [16], the pipeline retains some sensitivity, however, to nongeneral-relativity GW polarization models, including a longitudinal component, and to slow amplitude evolution.

The 95% confidence level upper limits (see Fig. 15) produced in the first stage are based on the overall noise level and largest outlier in strain found for every template in each 62.5 mHz band in the first stage of the pipeline. The 62.5 mHz bands are analyzed by separate instances of *PowerFlux* [16]. A follow-up search for detection is carried out for high-SNR outliers found in the first stage.

1. Universal statistics

As discussed above, a multitude of spectral combs contaminated the O1 low-frequency band, and, in contrast to the 23-month-long S5 Science Run and 15-month-long S6 Science Runs of initial LIGO, the 4-month-long O1 run did not span the Earth's full orbit. This means the Doppler shift magnitudes from the Earth's motion are reduced, on the whole, in O1 compared to those of the other, earlier runs. In particular, for certain combinations of sky location, frequency and spin-down, a signal can appear relatively stationary in frequency in the detector frame of reference. This effect is most pronounced for low signal frequencies, a pathology noted in searches of the 1-month-long S4 run [12]. At the same time, putative signals with low frequencies permit the use of 7200-s SFT spans, longer than the typical 1800-s SFTs used in the past, which helps to resolve stationary instrumental lines from signals. One downside, though, of longer coherence length is that there are far fewer SFTs in power sums compared with previous runs, which contributes to larger deviations from ideal Gaussian behavior for power-sum statistics.

To allow robust analysis of the entire spectrum, including the especially challenging lowest frequencies, the *universal statistic* algorithm [25] is used for establishing upper limits. The algorithm is derived from the Markov inequality and shares its independence from the underlying noise distribution. It produces upper limits less than 5% above optimal in case of Gaussian noise. In non-Gaussian bands, it can report values larger than what would be obtained if the distribution were known, but the upper limits are always at least 95% valid. Figure 1 shows results of an injection run performed as described in [16]. Correctly established upper limits lie above the red line.

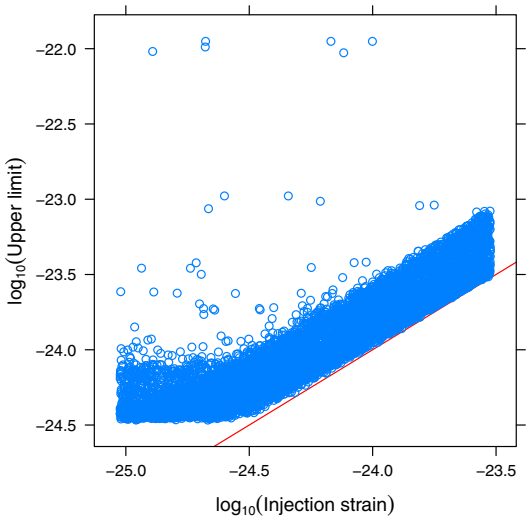

FIG. 1. *PowerFlux* upper limit validation. Each point represents a separate injection in the 50–200 Hz frequency range. Each established upper limit (vertical axis) is compared against the injected strain value (horizontal axis, red line).

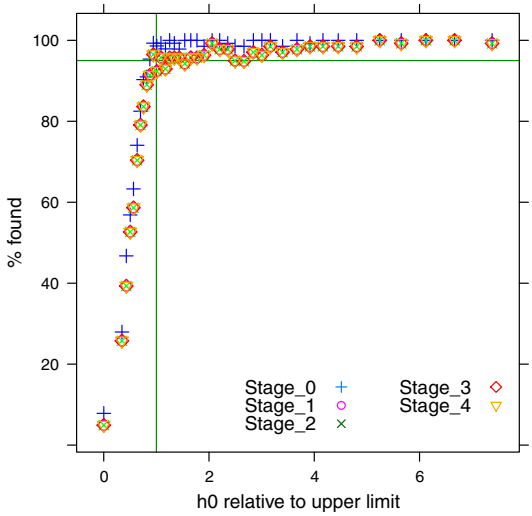

FIG. 2. *PowerFlux* injection recovery. The injections were performed in the 50–200 Hz band. The injected strain divided by the upper limit in this band (before injection) is shown on the horizontal axis. The percentage of surviving injections is shown on the vertical axis, with a horizontal line drawn at the 95% level. Stage 0 is the output of the coincidence test after the initial semicoherent search.

2. Outlier follow-up

The initial stage (labeled 0) scans the entire sky with the semicoherent *PowerFlux* algorithm that computes weighted sums of powers of 7200-s Hann-windowed SFTs. These power sums are then analyzed to identify high-SNR outliers. A separate algorithm uses the universal statistic [25] to establish upper limits.

The outlier follow-up procedure used in [16,20] has been extended with additional stages (see Table I) to reduce the larger number of initial outliers, expected because of non-Gaussian artifacts and larger initial search space.

The entire data set is partitioned into 3 stretches of equal length, and power sums are produced independently for any contiguous combinations of these stretches. As is done in [20,22], the outlier identification is performed independently in each stretch.

High-SNR outliers are subject to a coincidence test. For each outlier with SNR > 7 in the combined H1 and L1 data, we require there to be outliers in the individual detector data of the same sky area that had SNR > 5, matching the parameters of the combined-detector outlier within 83 μHz in frequency, and 7×10^{-11} Hz/s in spin-down. The combined-detector SNR is additionally required to be above both single-detector SNRs.

The identified outliers using combined data are then passed to the follow-up stage using the *Loosely Coherent* algorithm [24] with progressively tighter phase coherence parameters δ and improved determination of frequency, spin-down and sky location.

As the initial stage 0 sums only powers, it does not use the relative phase between interferometers, which results in some degeneracy among sky position, frequency and spin-down. The first *Loosely Coherent* follow-up stage also combines interferometer powers incoherently, but demands greater temporal coherence (smaller δ) within each interferometer, which should boost the SNR of viable outliers by at least 20%. Subsequent stages use data coherently, providing tighter bounds on outlier location.

Testing of the pipeline was performed for frequencies above 50 Hz. Injection recovery efficiencies from simulations covering the 50–200 Hz range are shown in Fig. 2. The same follow-up parameters were applied to the 20–50 Hz region, but with stage 0 utilizing twice as dense spin-down stepping.

Because the follow-up parameters were not tuned for the 20–50 Hz low frequency region and because of the highly disturbed spectrum, we do not expect a 95% recovery rate.

Only a mild influence from parameter mismatch is expected, as the parameters are chosen to accommodate the worst few percent of injections. The follow-up procedure establishes very wide margins for outlier follow-up. For example, when transitioning from the semicoherent stage 0 to the *Loosely Coherent* stage 1, the effective coherence length increases by a factor of 4. The average true signal SNR should then increase by more than 40%. But the threshold used in follow-up is only 20%, which accommodates unfavorable noise conditions, template mismatch and detector artifacts.

The follow-up code was verified to recover 95% of injections at or above the upper limit level for a uniform distribution of injection frequencies (Fig. 2).

The recovery criteria require that an outlier close to the true injection location (within 2 mHz in frequency f, 3×10^{-10} Hz/s in spin-down and 12 rad $\cdot$ Hz/f in sky

TABLE II. Properties of the FFTs used in the *FrequencyHough* pipeline. The time duration refers to the length in seconds of the data chunks on which the FFT is computed. The frequency bin width is the inverse of the time duration, while the spin-down bin width is computed as $\delta\dot{f} = \delta f/T_{\mathrm{obs}}$. In the analysis described in this paper only the first two bands have been considered.

Band [Hz]	Time duration [s]	δf [Hz]	$\delta\dot{f}$ [Hz/s]
[20–128]	8192	1.22×10^{-4}	1.18×10^{-11}
[128–512]	4096	2.44×10^{-4}	2.36×10^{-11}
[512–1024]	2048	4.88×10^{-4}	4.71×10^{-11}
[1024–2048]	1024	9.76×10^{-4}	9.42×10^{-11}

location) be found and successfully pass through all stages of the detection pipeline. As each stage of the pipeline passes only outliers with an increase in SNR, this resulted in simulated outliers that stood out strongly above the background, with good estimates of the parameters of the underlying signals.

B. *FrequencyHough* search method

The *FrequencyHough* method is described in detail in [23,37,38]. Calibrated detector data is used to create SFTs with coherence time depending on the frequency band being considered, see Table II. Short time-domain disturbances are removed from the data before constructing the SFTs [39]. A time-frequency map, called a peakmap, is built by selecting the local maxima (called peaks) over a threshold of 1.58 on the square root of the equalized power $\mathcal{R}(i) = \sqrt{\mathcal{P}(i)/S_{\mathrm{AR}}(i)}$, with $\mathcal{P}(i)$ being the value of the periodogram of the data at the frequency index i, and $S_{\mathrm{AR}}(i)$ an autoregressive estimation of the average power spectrum at the same frequency index [39] (then the index i runs along the full frequency band being considered). The peakmap is cleaned using a line "persistency" veto, described in [38], which consists of projecting the peakmap onto the frequency axis and removing the frequency bins in which the projection is higher than a given threshold.

After defining a grid in the sky, the peakmap for each sky position is corrected for the Doppler effect caused by the detector motion by shifting each peak to compensate for this effect. Shifted peaks are then fed to the *FrequencyHough* algorithm, transforming each peak to the frequency/spin-down plane of the source. The *FrequencyHough* algorithm is a particular implementation of the Hough transform, which is a robust parameter estimator of patterns in images. The frequency and spin-down bins depend on the frequency band, as indicated in Table II. The transformation properly weights any noise nonstationarity and the time-varying detector response [40].

The computation of the *FrequencyHough* transform is the most computationally demanding part of the analysis and needs to be split into thousands of independent jobs, each computing a *FrequencyHough* transform covering a small portion of the parameter space. In practice, each job covers 1 Hz, a small sky region—with a frequency-dependent size such that jobs at lower frequencies cover larger regions—and a range of spin-down values, as detailed below. The output of a *FrequencyHough* transform is a 2-D histogram in the frequency/spin-down plane of the source.

For each *FrequencyHough* histogram, candidates for each sky location are selected by dividing the 1-Hz band into 20 intervals and taking the most or (in most cases) the two most significant candidates for each interval, on the basis of the histogram number count. This is an effective procedure to avoid blinding by large disturbances in the data, which would contribute a large number of candidates if we used a toplist, i.e. if only candidates globally corresponding to the highest number count were selected. All the steps described thus far are applied separately to the data of each detector involved in the analysis.

Candidates from each detector are clustered and coincidence tests are applied between the two sets of clusters, using a distance metric built in the four-dimensional parameter space of position (λ, β) (in ecliptical coordinates), frequency f and spin-down $\dot{f}$, defined as

$$d_{\mathrm{FH}} = \sqrt{\left(\frac{\Delta f}{\delta f}\right)^2 + \left(\frac{\Delta \dot{f}}{\delta \dot{f}}\right)^2 + \left(\frac{\Delta \lambda}{\delta \lambda}\right)^2 + \left(\frac{\Delta \beta}{\delta \beta}\right)^2}, \quad (4)$$

where Δf, $\Delta \dot{f}$, $\Delta\lambda$ and $\Delta\beta$ are the differences, for each parameter, among pairs of candidates of the two detectors, and δf, $\delta \dot{f}$, $\delta\lambda$ and $\delta\beta$ are the corresponding bins, that is, the step width in a given parameter grid. Candidates within $d_{\mathrm{FH}} = 3$ are considered coincident. Coincident candidates are subject to a ranking procedure, based on the value of a statistic built using the distance and the *FrequencyHough* histogram weighted number count of the coincident candidates. More precisely, let us indicate with N the total number of coincident candidates in each 0.1-Hz band. First, candidates are ordered in descending order of the number count, separately for each data set, and a rank $r_{i,j}$ is assigned to each of them, from $1/N$ to the highest to 1 to the smallest, where $i = 1, 2$ identifies the data set and j runs over the coincident candidates of a given data set in a given 0.1-Hz band. Then, coincident candidates are ordered in ascending order of their distance, and a rank $r_{d,j}$ is assigned to each pair, going from $1/N$ for the nearest to 1 for the farthest. A final rank $r_j = r_{d,j} \times \prod_{i=1}^{2} r_{i,j}$ is computed and will take smaller values for more significant candidates, i.e. having smaller distance and higher number counts. A number of the most significant candidates are selected for each 0.1-Hz band and are subject to a follow-up procedure in order to confirm or reject them. This number depends on the amount of computing power which can be devoted to the follow-up. For the analysis described in this paper 4 candidates have been selected in each 0.1-Hz band.

1. Candidate follow-up

The follow-up consists of several steps (a detailed description is given in [23]). First, for each candidate, a fully coherent search using data from both detectors is performed assuming the parameters found for the candidate in this analysis. Although the coherent search corrects exactly for the Doppler and spin effect at a single particular point in the parameter space, corresponding to the candidate, the correction is extended, by linear interpolation, to the neighbors of the candidate. In practice, this means that from the resulting corrected and down-sampled time series, a new set of longer SFTs can be built, by a factor of 10 in this analysis, as well as a set of new (Doppler-corrected) peakmaps. The new peakmaps are valid even if the true signal parameters are slightly different from those of the candidate under consideration.

The joint corrected peakmaps (individually corrected for each detector's motion) are input to the *FrequencyHough* algorithm: overall, 1681 transforms are computed, covering ± 50 mHz, ± 1 spin-down bins (of initial width) and ± 0.75 bins (of initial width) for both λ and β around the candidate, and the loudest candidate among the full set of *FrequencyHough* maps is selected (note that the bin widths are now 10 times smaller than those of the initial stage of the analysis). The starting peakmap is then corrected using the parameters of the loudest candidate and projected on the frequency axis. We take the maximum of this projection in a range of ± 2 bins (of initial width) around the candidate frequency. We divide the rest of the 0.1-Hz band (which we consider the "off-source" region) into ~ 200 intervals of the same width, take the maximum of the peakmap projection in each of these intervals and sort in decreasing order all these maxima. We tag the candidate as "interesting" if it ranks first or second in this list.

Those candidates passing these tests are subject to further analysis: those candidates coincident with known noise lines (and that survived previous cleaning steps) are discarded, candidates with multi-interferometer significance less than the single-interferometer significance are discarded, candidates with single-interferometer significances differing by more than a factor of five are discarded, or candidates that have single-interferometer critical ratios ($\mathrm{CR} = (A_p - \mu_p)/\sigma_p$, with A_p being the candidate projection amplitude, μ_p and σ_p the mean and standard deviation of the projection) differing by more than a factor of five are discarded. The choice of this factor is a conservative one, validated by simulations, such that a detectable signal would not be vetoed at this stage. The outliers passing also these steps are subject to additional, manual scrutiny, see Sec. V C for more details concerning the O1 outliers.

As a validation of the follow-up we have made a study of software injection recovery. Specifically, we have generated about 110 signals which have been injected into representative 1-Hz bands, 64–65 Hz and 122–123 Hz, following the procedure described at the beginning of Sec. IV B 2 and with amplitude equal to the upper limit computed in those bands. The data has been analyzed with the *FrequencyHough* pipeline and candidates selected, as discussed in Sec. IV B. These candidates have been subject to the follow-up and all the candidates due to injected signals, i.e. within the standard follow-up volume around the corresponding injection, have been confirmed, showing a CR > 11 (to be compared with 7.57 which is the threshold used in the real analysis to select outliers, see Sec. V C). Moreover, we have verified that in most cases (about 90% of the cases in this test) the follow-up allows us to improve parameter estimation. In Figs. 3 and 4 we show the a-dimensional distance of candidates associated to simulated signals from their injection, defined by Eq. (4), both before and after the follow-up. The median of the distance reduces from 1.62 to 0.85 for the first band and from 1.55 to 0.88 for the second.

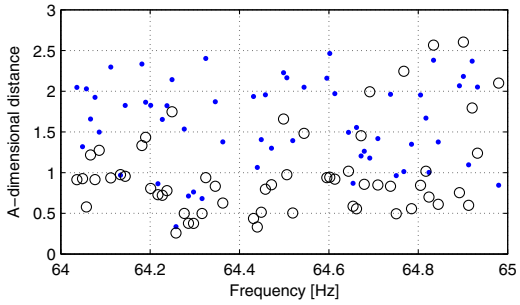

FIG. 3. A-dimensional distance between 56 injected signals in the band 64–65 Hz and the corresponding candidates (blue dots: before the follow-up; red circles: after the follow-up).

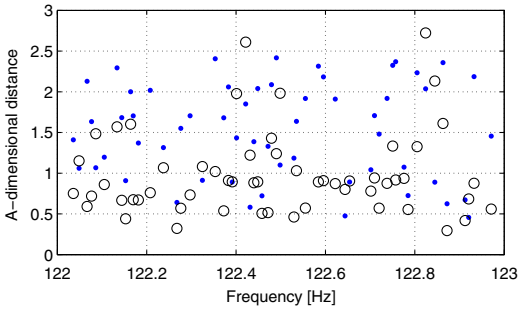

FIG. 4. A-dimensional distance between 57 injected signals in the band 122–123 Hz and the corresponding candidates (blue dots: before the follow-up; red circles: after the follow-up).

2. Upper limit computation

Upper limits are computed in each 1-Hz band between 20 Hz and 475 Hz by injecting software simulated signals, with the same procedure used in [23]. For each 1-Hz band 20 sets of 100 signals each are generated, with fixed amplitude within each set and random parameters (sky location, frequency, spin-down and polarization parameters). These are complex signals generated in the time

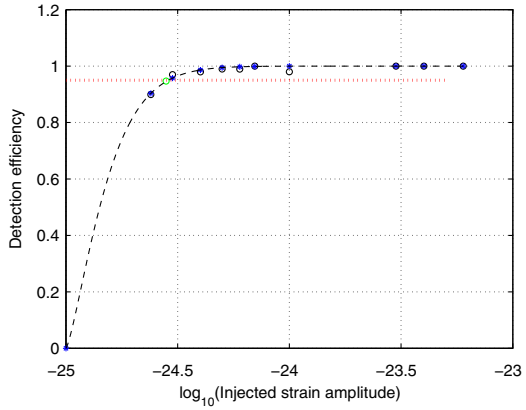

FIG. 5. Measured detection efficiency values for the band 423–424 Hz (circles) and their fit done using Eq. (5) (asterisks). The dashed line represents the full fitted curve. The dotted horizontal line indicates the 95% level of the detection efficiency.

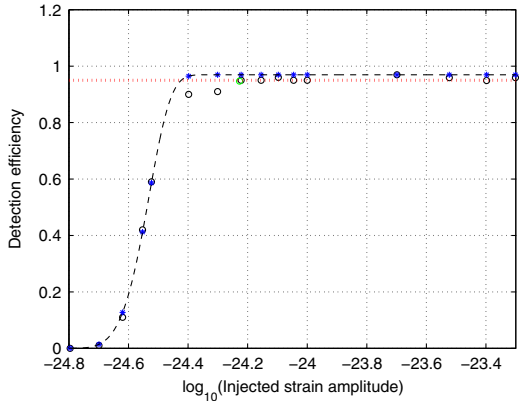

FIG. 6. Measured detection efficiency values for the band 51–52 Hz (circles) and their fit done using Eq. (5) (asterisks). The dashed line represents the full fitted curve. The dotted horizontal line indicates the 95% level of the detection efficiency.

domain at a reduced sampling frequency of 1 Hz, and then added to the data of both detectors in the frequency domain. For each injected signal in a set of 100, an analysis is done using the *FrequencyHough* pipeline over a frequency band of 0.1 Hz around the injection frequency, the full spin-down range used in the real analysis, and 9 sky points around the injection position [23]. Candidates are selected exactly as in the real analysis, but no clustering is applied because it would be affected by the presence of too many signals. Then, coincidences are required directly among candidates (clustering has been used mainly to reduce computational cost). Coincident candidates that are within the follow-up volume around the injection parameters and that have a critical ratio larger than the largest critical ratio found in the real analysis in the same band are considered as "detections" (excluding those that fall in a frequency bin vetoed by the persistency veto).

The upper limit in a given 1-Hz band is given by the signal amplitude such that 95% of the injected signals are detected. In practice, typically, a fit is used to the measured detection efficiency values in order to interpolate the detection efficiency when injections do not cover the 95% region densely enough. The fit has been done with the cumulative of a modified Weibull distribution function, given by

$$D(x) = K(1 - e^{-A_1(x-x_{\min})^{A_2}}), \tag{5}$$

where $x = \log_{10}(h_{\rm inj})$, $h_{\rm inj}$ is the injected amplitude, $x_{\min}$ is the value such that $D(x_{\min}) = 0$, K is a scaling factor such that the maximum of $D(x)$ is equal to the maximum measured detection efficiency, and A_1 and A_2 are the fit parameters. As an example, in Fig. 5 the measured detection efficiency values for the band 423–424 Hz are shown together with the fit. In cases like this, corresponding to artifact-free bands, the fit is accurate.

In more disturbed bands, the fit is not able to closely follow the measured values, as shown, for example, in Fig. 6. In such cases, if an interpolation is needed, a linear interpolation is used between the two detection efficiency points nearest (one from below and one from above) to the 95% level.

C. *SkyHough* search method

The *SkyHough* search method is described in detail in [18,41–43]. Calibrated detector $h(t)$ data from the O1 run is used to create 1800-s Tukey-windowed SFTs, where each SFT is created from a segment of detector data that is at least 1800 s long. From this step, 3684 and 3007 SFTs are created for H1 and L1, respectively. The data from the two LIGO interferometers are initially analyzed in separate all-sky searches for continuous gravitational wave signals, and then coincidence requirements on candidates are imposed.

SFT data from a single interferometer is analyzed by creating a peak-gram (a collection of zeros and ones) by setting a threshold of 1.6 on their normalized power. This is similar to the *FrequencyHough* method, but, in this case, the averaged spectrum is determined via a running-median estimation [12].

An implementation of the weighted Hough transform [18,42] is used to map points from the time-frequency plane of the peak-grams into the space of the source parameters. Similar to the methods described previously, the algorithm searches for signals whose frequency evolution fits the pattern produced by the Doppler shift and spin-down in the time-frequency plane of the data. In this case, the Hough number count is the weighted sum of the ones and zeroes, $n_k^{(i)}$, of the different peak-grams along the track corresponding to each point in parameter space. This sum is computed as

$$n = \sum_{i=0}^{N-1} w_k^{(i)} n_k^{(i)}, \tag{6}$$

where the choice of weights is optimal [42]. These weights are given by

$$w_k^{(i)} \propto \frac{1}{S_k^{(i)}} \{ (F_{+1/2}^{(i)})^2 + (F_{\times 1/2}^{(i)})^2 \}, \tag{7}$$

where $F_{+1/2}^{(i)}$ and $F_{\times 1/2}^{(i)}$ are the values of the antenna pattern functions at the mid-point of the i^{th} SFT for the sky location of interest and $S_k^{(i)}$ is the SFT noise level. A particularly useful detection statistic is the *significance* (or critical ratio), and is given by

$$s = \frac{n - \langle n \rangle}{\sigma}, \tag{8}$$

where $\langle n \rangle$ and σ are the expected mean and standard deviation of the Hough number count for pure noise.

The *SkyHough* search analyzes 0.1-Hz bands over the frequency interval 50–500 Hz, frequency time derivatives in the range $[-1.0, +0.1] \times 10^{-8}$ Hz/s, and covering the entire sky. A uniform grid spacing, equal to the size of a SFT frequency bin, $\delta f = 1/T_{\mathrm{coh}} = 5.556 \times 10^{-4}$ Hz is chosen, where T_{coh} is the duration of an SFT. The resolution $\delta \dot{f}$ is given by the smallest value of $\dot{f}$ for which the intrinsic signal frequency does not drift by more than one frequency bin during the total observation time T_{obs}: $\delta \dot{f} = \delta f / T_{\mathrm{obs}} \sim 4.95 \times 10^{-11}$ Hz s^{-1}. This yields 224 spin-down values for each frequency. The sky resolution $\delta\theta$ is frequency dependent, with the number of templates increasing with frequency, as given by Eq. (4.14) of Ref. [41], using a pixel factor of $N_p = 2$,

$$\delta\theta = \frac{10^4 \delta f}{f N_p}. \tag{9}$$

For each frequency band, the parameter space is split further into 209 subregions of the sky. For every sky region and frequency band the analysis program compiles a list of the 1000 most significant candidates. A final list of the 1000 most significant candidates per frequency band is constructed, with no more than 300 candidates from a single sky region. This procedure reduces the influence of instrumental spectral disturbances that affect specific sky regions.

The postprocessing of the results for each 0.1-Hz band consists of the following steps:

(i) Apply a χ^2 test, as described below, to eliminate candidates caused by detector artifacts.

(ii) Search for coincident candidates among the two data sets, using a coincidence window of $d_{\mathrm{SH}} < \sqrt{14}$. This dimensionless quantity, similar to the parameter d_{FH} used in the *FrequencyHough* pipeline, is defined as

$$d_{\mathrm{SH}} = \sqrt{(\Delta f/\delta f)^2 + (\Delta \dot{f}/\delta \dot{f})^2 + (\Delta\theta/\delta\theta)^2} \tag{10}$$

to take into account the distances in frequency, spin-down and sky location with respect to the grid resolution in parameter space. Here, $\Delta\theta$ is the sky angle separation. Each coincidence pair is then characterized by its harmonic mean significance value and a center in parameter space: the mean weighted value of frequency, spin-down and sky location obtained by using their corresponding individual significance values. Subsequently, a list containing the 1000 most significant coincident pairs is produced for each 0.1-Hz band.

(iii) The surviving coincidence pairs are clustered, using the same coincidence window of $d_{\mathrm{SH}} = \sqrt{14}$ applied to the coincidence centers. Each coincident candidate can belong to only a single cluster, and an element belongs to a cluster if there exists at least another element within that distance. Only the highest ranked cluster, if any, will be selected for each 0.1-Hz band. Clusters are ranked based on their mean significance value, but where all clusters overlapping with a known instrumental line are ranked below any cluster with no overlap. A cluster is always selected for each of the 0.1-Hz bands that had coincidence candidates. In most cases the cluster with the largest mean significance value coincides also with the one containing the highest value.

Steps (ii) and (iii) take into account the possibility of coincidences and formation of clusters across boundaries of consecutive 0.1-Hz frequency bands. The following tests are performed on those candidates remaining:

(iv) Based on previous studies [26], we require that interesting clusters must have a minimum population of 6 and that coincidence pairs should be generated from at least 2 different candidates per detector.

(v) For those candidates remaining, a multidetector search is performed to verify the consistency of a possible signal. Any candidate that has a combined significance more than 1.6 below the expected value is discarded.

Outliers that pass these tests are manually examined. In particular, outliers are also discarded if the frequency span of the cluster coincides with the list of narrow instrumental lines described in Sec. II, or if there are obvious spectral disturbances associated with one of the detectors.

1. The χ^2 veto

The χ^2 test was first implemented in the *SkyHough* analysis of initial LIGO era S5 data [18], and is used to reduce the number of candidates from single-interferometer analysis before the coincidence step. A veto threshold for the χ^2 test is derived empirically from the O1 SFT data set. A large number of simulated periodic gravitational wave signals are added to the SFTs, with randomly chosen amplitude, frequency, frequency derivative, sky location, polarization angle, inclination angle and initial phase. Then, the data is analyzed separately for each detector, H1 and L1.

To determine the χ^2 veto threshold (characterized by a "veto curve"), 125 0.1-Hz bands are selected for H1 and 107 bands for L1, bands free of known large spectral disturbances. In total, 2,340,000 injections are analyzed. The χ^2 values are defined with respect to a split of the SFT data into $p = 16$ segments. The results are sorted with respect to the significance and grouped in sets containing 2000 points. For each set the mean value of the significance, the mean of the χ^2 and its standard deviation are computed. With this reduced set of points, we fit two power laws, $p - 1 + A_1 s^{A_2}$ and $\sqrt{2p-2} + B_1 s^{B_2}$, to the mean and standard deviation curve.

A detailed study of the calibration of the χ^2 test using LIGO O1 data can be found in [44]. This study revealed a frequency-dependent behavior. In particular, the results obtained from injections below 100 Hz differ from those between 100 and 200 Hz, while the characterization of the χ^2-significance plane was similar for frequencies higher than 200 Hz. For this reason, three different veto curves have been derived for the 50–100 Hz band, 100–200 Hz band and for frequencies higher than 200 Hz. In the corresponding frequency bands, the characterization was similar for both interferometers. Therefore, common veto curves are derived.

The coefficients obtained for the proposed characterization can be found in Table III. Figures 7, 8 and 9 show the fitted curves and resulting veto curves corresponding veto for the mean χ^2 plus five times its standard deviation for the H1-L1 combined data. The associated false dismissal rate for this veto is measured to be 0.12% for the 50–100 Hz band, 0.21% for the 100–200 Hz band and 0.16% for frequencies higher than 200 Hz.

TABLE III. Parameters obtained for the O1 χ^2 veto curve characterization in different frequency bands.

f [Hz]	A_1	A_2	B_1	B_2
50–100	0.4902	1.414	0.3581	1.481
100–200	0.2168	1.428	0.1902	1.499
> 200	0.1187	1.470	0.0678	1.697

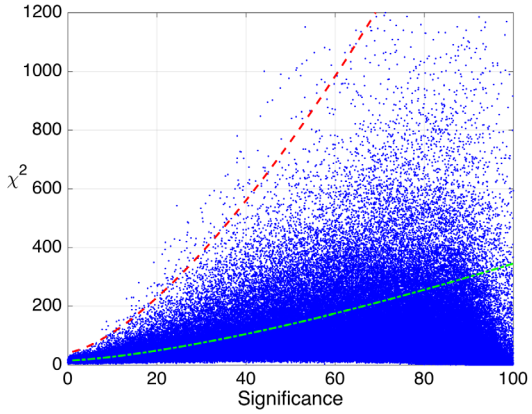

FIG. 7. Significance-χ^2 plane for 180000 simulated injected signals in the 50–100 Hz band together with the fitted mean curve (dotted-dashed line) and the veto curve (dashed line) corresponding to the mean χ^2 plus five times its standard deviation for the H1-L1 combined data. The associated false dismissal rate (percentage of injections that are higher than the veto curve) is measured to be 0.12%.

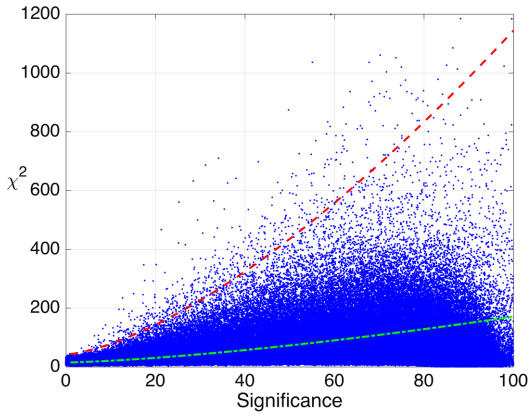

FIG. 8. Same as Fig. 7 for 320000 injections in the 100–200 Hz band. The false dismissal rate is 0.21%.

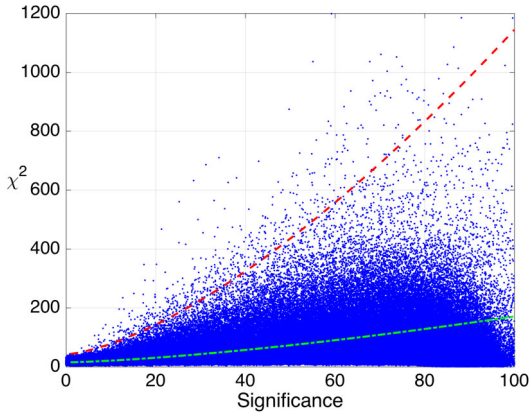

FIG. 9. Same as Fig. 7 for 1840000 injections at frequencies higher than 200 Hz for the combined H1-L1 data. The false dismissal rate is 0.16%.

2. The multidetector consistency veto

Similar to the preceding χ^2 test, a multidetector consistency veto can be derived by comparing the significance results from a multidetector search to those obtained by analyzing the data from the H1 and L1 detectors separately.

In particular, for each point in parameter space, we can derive the expected multidetector significance from the significance obtained in the separate analysis of H1 and L1 data by using the weights defined by Eq. (7) and the SFT sets in use. Since in this search the exact value of the weights is not stored, an approximation can be derived by ignoring the effect of the antenna pattern and considering only the influence of the varying noise levels of the different SFTs in a given frequency band.

The following expression can then be derived for the multidetector search:

$$s_{\text{theo}} = \frac{s_{\text{L1}}\sqrt{\sum_{i=0}^{N_{\text{L1}}}\left(S_{\text{L1}}^{(i)}\right)^{-2}} + s_{H1}\sqrt{\sum_{i=0}^{N_{\text{H1}}}\left(S_{\text{H1}}^{(i)}\right)^{-2}}}{\sqrt{\sum_{i=0}^{N_{\text{L1}}}\left(S_{\text{L1}}^{(i)}\right)^{-2} + \sum_{i=0}^{N_{\text{H1}}}\left(S_{\text{H1}}^{(i)}\right)^{-2}}}, \quad (11)$$

where N_{H1} and N_{L1} are the number of SFTs of each detector, $S_{\text{H1}}^{(i)}$ and $S_{\text{L1}}^{(i)}$ are the one-sided PSDs of each detector averaged around a small frequency interval and s_{H1} and s_{L1} are the significances of the separate single-detector searches.

Ideally, a coincidence pair from a periodic gravitational wave signal would have s_{H1}, s_{L1} and s_{theo} values consistent with Eq. (11) within uncertainties arising from use of nearby —but not identical—templates and from noise fluctuations. Furthermore, we are interested in characterizing its validity when considering the maximum significance values obtained in a small volume in parameter space.

In order to test the validity of the consistency requirement, we have injected simulated signals in the 50–500 Hz range, randomly covering the same parameters of our search and for a variety of signal amplitudes. A full search, but covering only one sky patch, is performed on H1 and L1 data, as well as for the combined SFT data, returning a list of the most significant candidates for each of them. Of all the injections performed, we considered only those with amplitudes strong enough that within a frequency and spin-down window of 4 bins around the injected signal parameters, the maximum significance value would be at least 5 for both individual single-interferometer searches, and consequently a theoretical combined significance higher than 7. A total of 4356 injections with an expected theoretical combined significance between 7 and 50 were considered, and the results are presented in Fig. 10.

In Fig. 10 we characterize the difference in significance obtained with respect to the theoretical expected value. From this plot, the multidetector consistency veto for the O1 data used in this search can be determined: if the multidetector combined significance has a value more than 1.6 below the nominal theoretically expected value, the candidate is vetoed. This value of 1.6 yields a false dismissal rate of 0.07%.

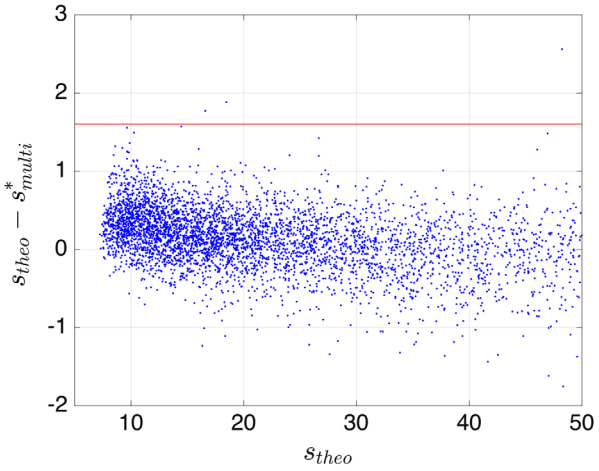

FIG. 10. Characterization of the multidetector significance consistency veto using 4356 simulated injected signals in the 50–500 Hz range. Each point represents a separate injection. The horizontal axis corresponds to the theoretical expected significance value, s_{theo}, while the vertical axis is the difference between the theoretical and the measured value of significance, s^*_{multi}. The solid line is placed at a difference in significance of 1.6 that has only been exceeded by 3 injections.

3. Upper limit computation

Upper limits are derived from the sensitivity depth for each 0.1-Hz band between 50 and 500 Hz. The value of the depth corresponding to the averaged 95% confidence level upper limit is obtained by means of simulated periodic gravitational wave signals added into the SFT data of both detectors H1 and L1 in a limited number of frequency bands. In those bands, the detection efficiency, i.e. the fraction of signals that are considered detected [that have passed steps (i)–(iv) above], is computed as a function of signal strength, h_0 expressed by the sensitivity depth $\sqrt{S_n}/h_0$ $(1/\sqrt{\text{Hz}})$. Here, S_n is the maximum over both detectors of the power spectral density of the data, at the frequency of the signal, estimated as the power-2 mean value, $\left(\sum_{i=1}^{N}\left(S_k^{(i)}\right)^{-2}/N\right)^{-2}$, across the different noise level $S_k^{(i)}$ of the different N SFTs.

Twenty-two different 0.1-Hz bands free of spectral disturbances in both detectors were selected with the following starting frequencies: 73.6, 80.8, 98.3, 140.8, 170.2, 177.8, 201.1, 215.1, 240.7, 240.8, 250.7, 305.3, 320.3, 350.6, 381.6, 400.7, 402.1, 406.8, 416.2, 436.9, 446.9, 449.4. In all these selected bands, we generated five sets of 200 signals each, with fixed sensitivity depth each set and random parameters $(f, \alpha, \delta, \dot{f}, \varphi_0, \psi, \cos\iota)$. For each injected signal added into the data of both detectors

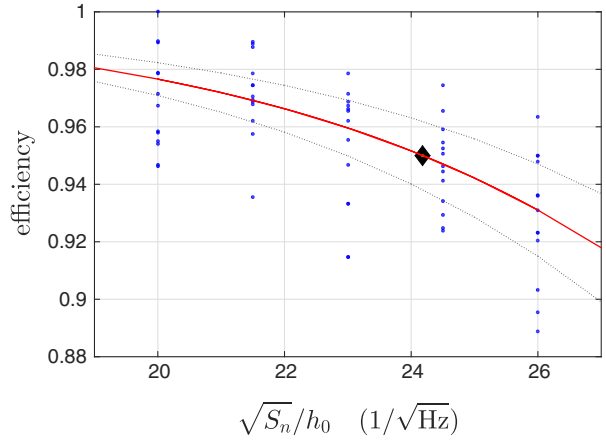

FIG. 11. Detection efficiency as a function of depth obtained for 22 frequency bands. Each dot corresponds to a set of 200 signal injections. The solid line (red) corresponds to the fitted sigmoid curve. The diamond shows the depth value corresponding to an averaged all-sky 95% detection efficiency, $D^{95\%} = 24.2\ (1/\sqrt{\text{Hz}})$.

an analysis was done using the *SkyHough* search pipeline over a frequency band of 0.1 Hz and the full spin-down range, but covering only one sky patch. For this sky patch a list of 300 loudest candidates was produced. Then we imposed a threshold on significance, based on the minimum significance found in the all-sky search in the corresponding 0.1-Hz band before any injections. The postprocessing is then done using the same parameters as in the search, including the population veto.

For each of those 22 frequency bands, a sigmoid curve,

$$\text{Efficiency}(\text{Depth}) = 1 - \frac{1}{1 + \exp(b(\text{Depth} - a))}, \qquad (12)$$

was fitted by means of the least absolute residuals. Then the 95% confidence upper limit was deduced from the corresponding value of the depth. With this procedure, the minimum and maximum values of the depth corresponding to the desired upper limit were 21.9 and 26.6 $(1/\sqrt{\text{Hz}})$, respectively. We also collected the results from all the frequency bands and, as shown in Fig. 11, performed a sigmoid fitting as before and obtained the following fitted coefficients (with 95% confidence bounds): $a = 39.83$ (34.93, 44.73) $(1/\sqrt{\text{Hz}})$ and $b = -0.1882$ $(-0.2476, -0.1289)$ $(\sqrt{\text{Hz}})$, which yields the joint depth for corresponding to the 95% upper limit of $D^{95\%} = 24.2\ (1/\sqrt{\text{Hz}})$, its uncertainty being smaller than 7% for undisturbed bands, with the exception of the 98.3-Hz band for which the upper limit using this joint value would be underestimated by 10% and for the 406.8-Hz band for which the upper limit is overestimated by 9.5%.

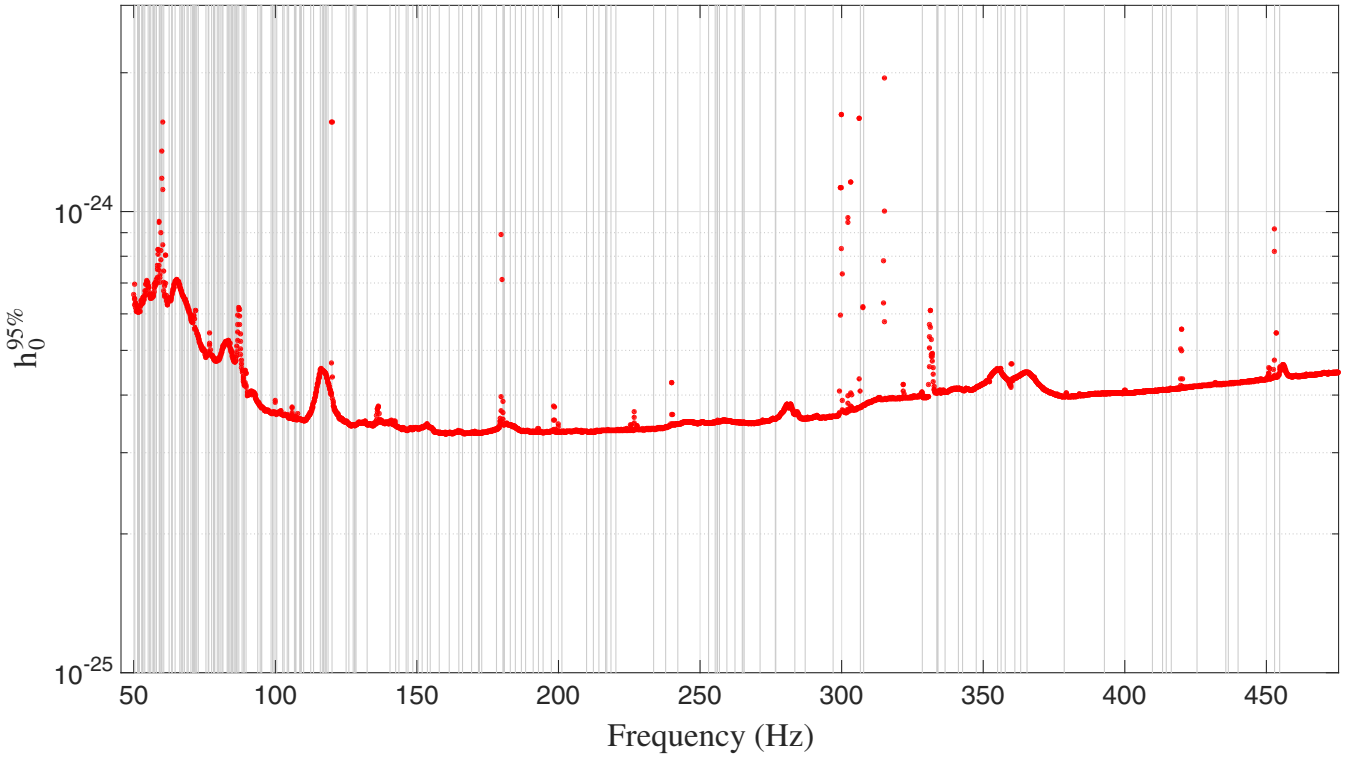

FIG. 12. *SkyHough* O1 upper limits. The dotted (red) curve shows the averaged 95% confidence level upper limits for every analyzed 0.1-Hz band. The vertical (grey) lines indicate 194 0.1-Hz bands in which coincidence candidates were found and consequently no upper limits are set.

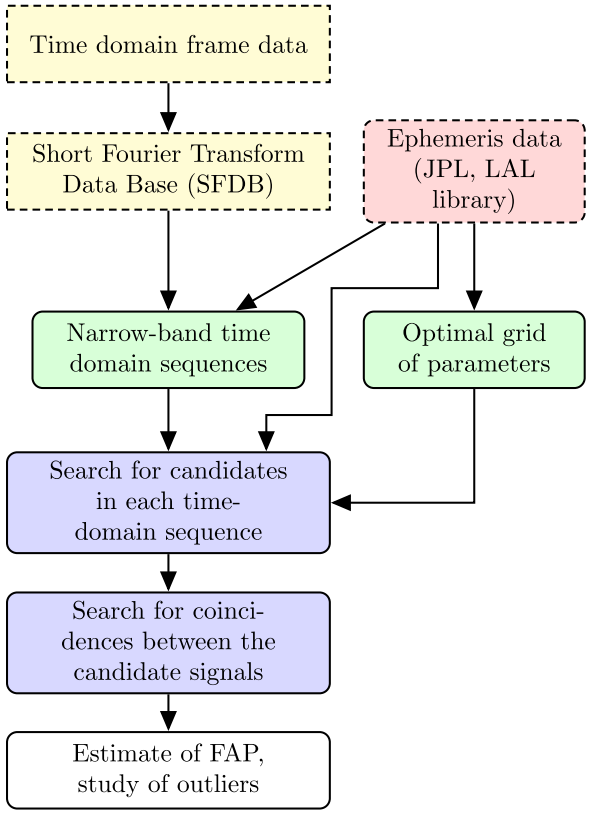

FIG. 13. *Time-Domain $\mathcal{F}$-statistic* pipeline flowchart. Two main parts of the pipeline are the coherent $\mathcal{F}$-statistic search for candidate signals in time-domain segments, which is followed by a search for coincidences between candidates from different time-domain segments.

The 95% confidence upper limit on h_0 for undisturbed bands can then be derived by simply scaling the power spectral density of the data, $h_0^{95\%} = \sqrt{S_n}/D^{95\%}$. The computed upper limits are shown in Fig. 12. No limits have been placed in 194 0.1-Hz bands in which coincidence candidates were detected, as this scaling procedure can have larger errors in those bands due to the presence of spectral disturbances.

D. *Time-Domain $\mathcal{F}$-statistic* search method

The *Time-Domain $\mathcal{F}$-statistic* search method uses the algorithms described in [19,27,45,46] and has been applied to an all-sky search of VSR1 data [19].

The search method consists primarily of two parts. The first part is the coherent search of narrowband, time-domain segments. The second part is the search for coincidences among the candidates obtained from the coherent search (see Fig. 13).

The time-domain segments of the data are extracted from the same set of SFTs used by the *FrequencyHough* pipeline. The data are split into bands 0.25 Hz long. The bands are overlapped by 2×10^{-7} Hz. For each band, the data is inverse Fourier transformed to extract a time series of O1 data from the SFTs. The time series is divided into segments, called frames, of 6 sidereal days each. Thus, the band [10–475] Hz has 1921 frequency bands. The band number b is related to the reference band frequency f_b as follows:

$$f_b = 10\ \text{Hz} + \frac{b(1-2^{-5})}{2\Delta t}, \tag{13}$$

where the sampling time $\Delta t = 2$ s. For O1 data, which is about 120 days long, we obtain 20 time frames. Each 6-day narrowband segment contains $N = 258492$ data points. The O1 data has a number of nonscience data segments. The values of these bad data are set to zero. For analysis, we choose only segments that have a fraction of bad data less than $1/3$. This requirement results in eight 6-day-long data segments for each band. Consequently, we have 15368 data segments to analyze. These segments are analyzed coherently using the $\mathcal{F}$-statistic. We set a fixed threshold for the $\mathcal{F}$-statistic of $\mathcal{F}_0 = 14.5$ and record parameters of all the threshold crossings together with the corresponding values of the signal-to-noise ratio ρ,

$$\rho = \sqrt{2(\mathcal{F} - 2)}. \tag{14}$$

For the search we use a four-dimensional (parametrized by frequency, spin-down and two more parameters related to the position of the source in the sky) grid of templates constructed in Sec. IV of [46], which belongs to the family S_1 of grids considered in [46]. The grid has a minimal match $\text{MM} = \sqrt{3}/2$ and its thickness equals 1.77959, which is only ∼0.8% larger than the thickness of the four-dimensional optimal lattice covering A_4^* (equal to 1.76553). We also veto candidates overlapping with lines identified as instrumental artifacts.

In the second stage of the search we search for coincidences among the candidates obtained in the coherent part of the search. We use exactly the same coincidence search algorithm as in the analysis of VSR1 data and described in detail in Section VIII of [19]. We search for coincidences in each of the 1921 bands analyzed. To estimate the significance of a given coincidence, we use the formula for the false alarm probability derived in the appendix of [19]. Sufficiently significant coincidences are called outliers and subject to further investigation.

1. Sensitivity of the search

The sensitivity of the search is taken to be the amplitude h_0 of the gravitational wave signal that can be confidently detected. To estimate the sensitivity we use a procedure developed in [13]. We determine the sensitivity of the search in each of the 1921 frequency bands that we have searched. We perform Monte Carlo simulations in which, for a given amplitude h_0, we randomly select the other seven parameters of the signal: $\omega_0, \omega_1, \alpha, \delta, \phi_0, \iota$ and ψ. We

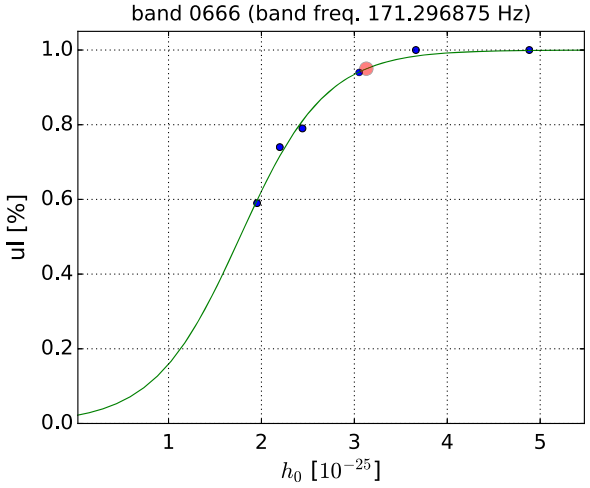

FIG. 14. *Time-Domain $\mathcal{F}$-statistic* method of establishing upper limits from the Monte Carlo simulations with sigmoid fitting (an example for band No. 0666). Blue dots denote the results of the MC simulations for the range of amplitudes h_0 of injected signals with otherwise randomly chosen parameters. The green curve is the best fit of Eq. (15); the red dot corresponds to the 95% upper limit (see Fig. 18 for the summary of results for the whole range of searched frequencies).

choose frequency and spin-down parameters uniformly over their range, and source positions uniformly over the sky. We choose angles ϕ_0 and ψ uniformly over the interval $[0, 2\pi]$ and $\cos\iota$ uniformly over the interval $[-1, 1]$. For each band, the simulated signal is added to all the data segments chosen for the analysis in that band. Then the data is processed through the pipeline.

First, we perform a coherent $\mathcal{F}$-statistic search of each of the data segments where the signal was added, and store all the candidates above a chosen $\mathcal{F}$-statistic threshold of 14.5. In this coherent analysis, to make the computation manageable, we search over a limited parameter space consisting of ± 2 grid points around the nearest grid point where the signal was added. Then the coincidence analysis of the candidates is performed. The signal is considered to be detected, if it is coincident in more than 5 of the 8 time frames analyzed for a given band. The ratio of numbers of cases in which the signal is detected to the total number of simulations performed for a given h_0 determines the frequentist sensitivity upper limits. To obtain the 95% confidence sensitivity limit on h_0 we fit a sigmoid function,

$$S(x) = \frac{1}{1 + e^{k(x_0 - x)}}, \tag{15}$$

to these data, with x_0 and k being the fitted parameters. An example result, for a band frequency 171.296875 Hz (corresponding to band number 0666) is presented in Fig. 14. The 95% confidence upper limits for the whole range of frequencies are given in Fig. 18; they follow very well the noise curves of the O1 data that were analyzed.

V. SEARCH RESULTS

A. Introduction

Results from the four search pipelines are presented below. In summary, no pipelines found a credible gravitational wave signal after following up initial outlier candidates, and each pipeline obtained a set of upper limits. In a number of bands, particularly at low frequencies, instrumental artifacts prevented setting of reliable upper limits. The sensitivities obtained by the different pipelines are comparable and generally in line with expectations from the previous mock data challenge that used data from the Initial LIGO S6 run [26], but a greater density of instrumental artifacts in the O1 data and refined algorithm parameter choices led to additional small performance differences in this analysis. In addition to the upper limit graphs presented below, numerical data for these values can be obtained separately [47].

B. *PowerFlux* search results

The *PowerFlux* algorithm and *Loosely Coherent* method compute power estimates for continuous gravitational waves in a given frequency band for a fixed set of templates. The template parameters usually include frequency, first frequency derivative and sky location.

Since the search target is a rare monochromatic signal, it would contribute excess power to one of the frequency bins after demodulation. The upper limit on the maximum excess relative to the nearby power values can then be established. For this analysis we use a universal statistic [25] that places conservative 95% confidence level upper limits for an arbitrary statistical distribution of noise power. The universal statistic has been designed to provide close to optimal values in the common case of Gaussian distribution.

The upper limits obtained in the search are shown in Fig. 15. The upper (yellow) curve shows the upper limits for a worst-case (linear) polarization when the smallest amount of gravitational energy is emitted toward the Earth. The lower curve shows upper limits for an optimally oriented source (circular polarization). Because of the day-night variability of the interferometer sensitivity due to anthropogenic noise, the linearly polarized sources are more susceptible to detector artifacts, as the detector response to such sources varies with the same period.

Each point in Fig. 15 represents a maximum over the sky, except for a small excluded portion of the sky near the ecliptic poles, which is highly susceptible to detector artifacts due to stationary frequency evolution produced by the combination of frequency derivative and Doppler shifts. The exclusion procedure is described in [16] and applied to 0.2% of the sky over the entire run.

If one assumes that the source spin-down is solely due to emission of gravitational waves, then it is possible to

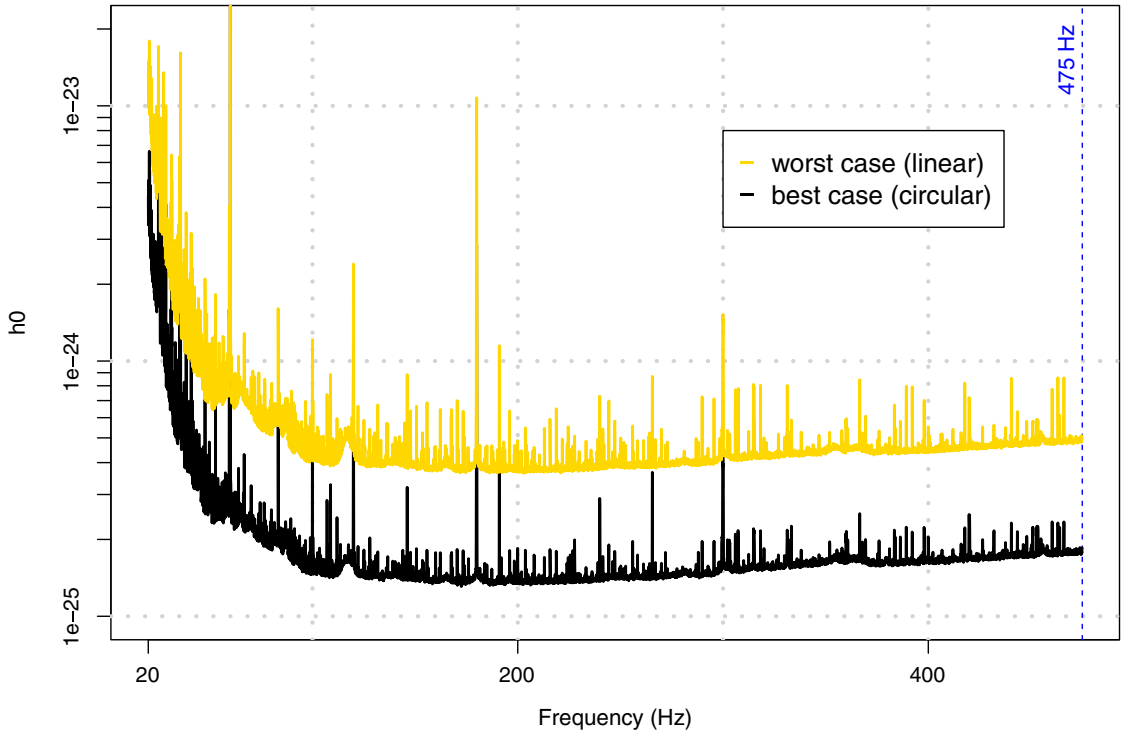

FIG. 15. *PowerFlux* O1 upper limits. The upper (yellow) curve shows worst-case (linearly polarized) 95% CL upper limits in analyzed 62.5 mHz bands. The lower (grey) curve shows upper limits assuming a circularly polarized source. The data for this plot can be found in [47].

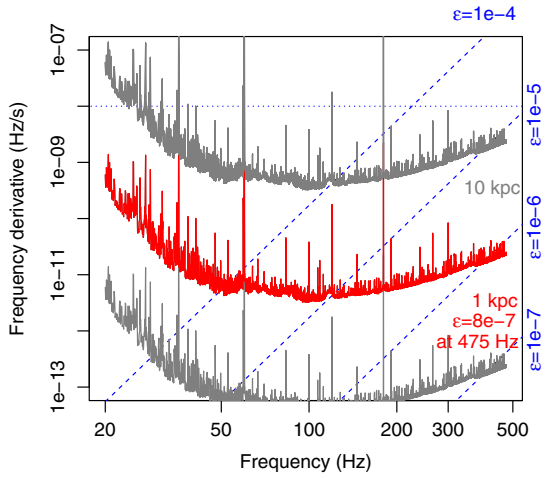

FIG. 16. Range of the *PowerFlux* search for neutron stars spinning down solely due to gravitational radiation. This is a superposition of two contour plots. The grey and red solid lines are contours of the maximum distance at which a neutron star could be detected as a function of gravitational wave frequency f and its derivative $\dot{f}$. The dashed lines are contours of the corresponding ellipticity $\epsilon(f,\dot{f})$. The fine dotted line marks the maximum spin-down searched. Together these quantities tell us the maximum range of the search in terms of various populations (see text for details). The other three search pipelines have similar ranges for circularly polarized sources.

recast upper limits on source amplitude as limits on source ellipticity. Figure 16 shows the reach of the *PowerFlux* search under different assumptions on source distance for circularly polarized signals. Superimposed are lines corresponding to sources of different ellipticities. Although not presented here, corresponding maximum ranges for circularly polarized sources derived from the strain upper limits of the other three pipelines would be similar.

The detection pipeline produced 62 outliers located near a 0.25-Hz comb of detector artifacts (Table X), 74 outliers spanning only one data segment (about 1 month) which are particularly susceptible to detector artifacts (Table IX) and 25 outliers (Table VIII) that do not fall into either of those two categories. Each outlier is identified by a numerical index. We report here SNR, frequency, spin-down and sky location.

The "Segment" column describes the persistence of the outlier through the data, and specifies which contiguous subset of the three equal partitions of the timespan contributed most significantly to the outlier: see [22] for details. A true continuous signal from an isolated source would normally have [0,2] in this column (similar contributions from all three segments), or on rare occasions [0,1] or [1,2]. Any other range strongly suggests a statistical fluctuation, an artifact or a signal that does not conform to the phase evolution of Equation (2).

TABLE IV. Parameters of the hardware-injected simulated continuous-wave signals during the O1 data run (epoch GPS 1130529362). Because the interferometer configurations were largely frozen in a preliminary state after the first discovery of gravitational waves from a binary black hole merger, the hardware injections were not applied consistently. There were no injections in the H1 interferometer initially, and the initial injections in the L1 interferometer used an actuation method with significant inaccuracies at high frequencies.

Label	Frequency Hz	Spin-down nHz/s	RA_{J2000} degrees	DEC_{J2000} degrees
ip0	265.575533	-4.15×10^{-3}	71.55193	−56.21749
ip1	848.969641	-3.00×10^{-1}	37.39385	−29.45246
ip2	575.163521	-1.37×10^{-4}	215.25617	3.44399
ip3	108.857159	-1.46×10^{-8}	178.37257	−33.4366
ip4	1393.540559	-2.54×10^{-1}	279.98768	−12.4666
ip5	52.808324	-4.03×10^{-9}	302.62664	−83.83914
ip6	146.169370	-6.73×10^{0}	358.75095	−65.42262
ip7	1220.555270	-1.12×10^{0}	223.42562	−20.45063
ip8	191.031272	-8.65×10^{0}	351.38958	−33.41852
ip9	763.847316	-1.45×10^{-8}	198.88558	75.68959
ip10	26.341917	-8.50×10^{-2}	221.55565	42.87730
ip11	31.424758	-5.07×10^{-4}	285.09733	−58.27209
ip12	38.477939	-6.25×10^{0}	331.85267	−16.97288
ip13	12.428001	-1.00×10^{-2}	14.32394	−14.32394
ip14	1991.092401	-1.00×10^{-3}	300.80284	−14.32394

During the O1 run several simulated pulsar signals were injected into the data by applying a small force to the interferometer mirrors with auxiliary lasers or via inductive forces from nearby electrodes [48]. Several outliers were due to such hardware injections (Table IV). The hardware injection ip3 was exceptionally strong, with a clear signature even in its non-Gaussian band. Note, however, that these injections were not enabled for the H1 interferometer in the first part of the O1 run, leading to degraded efficiency for their detections.

The recovery of the hardware injections gives us additional confidence that no potential signals were missed. Manual follow-up has shown noninjection outliers spanning all three segments to be caused by pronounced detector artifacts. Several outliers (numbers 47, 56, 70, 72, 134, 138, 154 in Table VIII) spanning two segments were also investigated with a fully coherent followup based on the Einstein@Home pipeline [31,32]. None was found to be consistent with the astrophysical signal model. Tables with more details may be found in Appendix A.

C. *FrequencyHough* search results

In this section we report the main results of the O1 all-sky search using the *FrequencyHough* pipeline. The number of initial candidates produced by the Hough transform stage was about 4.79×10^9 (of which about 2.58×10^8 belong to the band 20–128 Hz, and the rest to the band 128–512 Hz) for both Hanford and Livingston detectors. As the number of coincident candidates remained too large, 231475 for the band 20–128 Hz and 3109841 for the band 128–512 Hz, we reduced it with the ranking procedure described in Sec. IV B. In practice, for computational efficiency reasons all the analysis was carried out separately for two different spin-down ranges: one from $+10^{-9}$ Hz/s to -2×10^{-9} Hz/s and the other from -2×10^{-9} Hz/s to -10^{-8} Hz/s. As a consequence, the number of candidates selected after the ranking was 8640 for the band 20–128 Hz and 30720 for the band 128–512 Hz. Each of these candidates was subject to the follow-up procedure, described in Sec. IV B 1. The number of candidates passing the first follow-up stage was 273 for the band 20–128 Hz and 1307 for the band 128–512 Hz and, after further vetoes, reduced to 64 for the band 20–128 Hz and 496 for the band 128–512 Hz.

From these surviving candidates we selected the outliers less consistent with noise fluctuations. In particular, we chose those for which the final peakmap projection has a critical ratio $CR > 7.57$. This is the threshold corresponding to a false alarm probability of 1% on the noise-only distribution after having taken into account the look-elsewhere effect (on the follow-up stage) [49]. The list of outliers is shown in Table XI. Each of these outliers has been manually examined, and for all of them a gravitational wave origin could be excluded, as discussed in Appendix B.

Upper limits have been computed in 1-Hz bands, as described in Sec. IV B 2 and are shown in Fig. 17. The minimum value is about 2.5×10^{-25}, reached in the range 150–200 Hz. In a number of frequency bands the upper limit value deviates from the smooth underlying distribution. This is a consequence of the typical behavior we see in disturbed bands and shown, as an example, in Fig. 6: when the measured detection efficiency does not closely follow the Weibull fitting function [see Eq. (5)] in the interval around the 95% level, the resulting upper limit can be significantly larger with respect to the value expected for a quiet band. We have verified that such fluctuations could be significantly reduced by increasing the number of candidates selected at the ranking level: for instance, going from 4 to 8 would yield much smoother results (at the price of doubling the number of follow-ups to be done). There are some highly disturbed bands, especially below 40 Hz, for which we are unable to compute the upper limit because the detection efficiency never reaches the 95% level.

As a further test of the capabilities of the pipeline to recover signals, in addition to those shown in Sec. IV B 1, we report in Table V parameters of the recovered hardware injections, together with the error with respect to the injected signals. In general, we find a good agreement (with the exception of ip5 and ip12, which are missed).

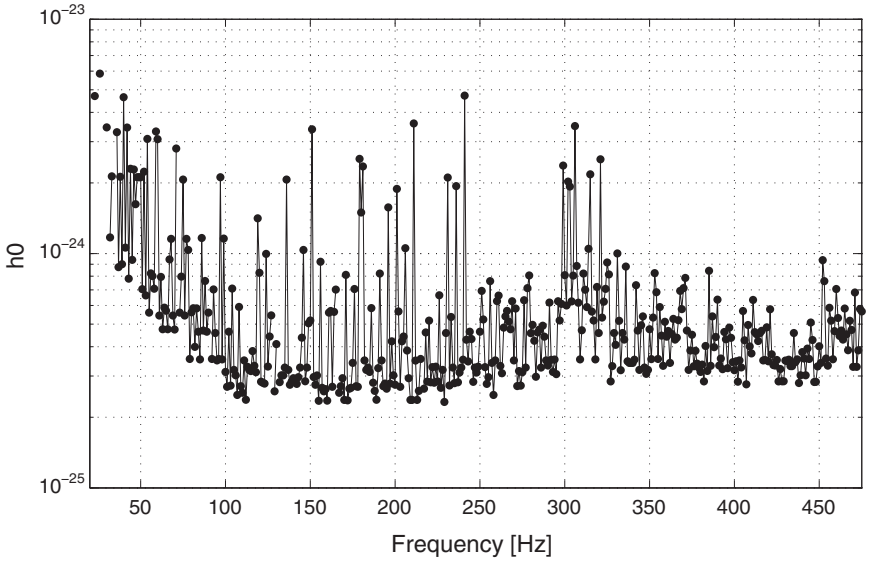

FIG. 17. Upper limits for the *FrequencyHough* pipeline, in the range between 20 Hz and 475 Hz.

D. *SkyHough* search results

In this section we report the main results of the O1 all-sky search between 50 and 500 Hz using the *SkyHough* pipeline, as described in Sec. IV C. In total, 194 0.1-Hz bands contained coincidence candidates, and therefore 194 coincidence clusters were identified and further investigated. The majority of these outliers corresponded to known spectral lines, severe spectral disturbances or hardware injected signals.

This initial list was reduced to 59 after applying the cluster population veto and to 26 after the multi-interferometer consistency veto. A detailed list of these remaining outliers is shown in Table XII. The multi-interferometer significance consistency veto alone was able to reduce the initial list of 194 candidates to 33.

Of these 26 outliers, 5 corresponded to hardware injected pulsars and 20 to known line artifacts contaminating either H1 or L1 data. The only unexplained outlier around 452.89989 Hz is due to an unknown large spectral disturbance in the H1 detector. Table VI provides details on outliers corresponding to hardware injections.

Therefore, this search did not find any evidence of a continuous gravitational wave signal. Upper limits have

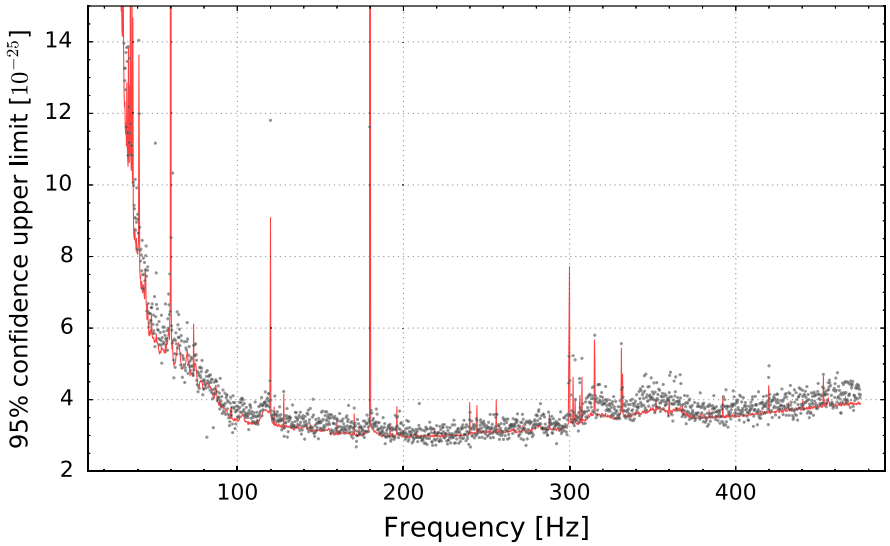

FIG. 18. *Time-Domain $\mathcal{F}$-statistic* pipeline O1 upper limits. Black dots are the 95% confidence upper limits for each frequency; the red line denotes the H1 and L1 detectors' average noise curve rescaled by the factor $27.5/\sqrt{T_0}$, where $T_0 = 516984$ s is the observational time of the 6-day time series segment.

TABLE V. Hardware injection recovery with the *FrequencyHough* pipeline. The reported values have been obtained at the end of the full analysis, including the follow-up. The values in parentheses are the absolute errors, that is, the difference with respect to the injection parameters. The reference time is MJD = 57328.59684. Two hardware injections are not accurately found (and not reported in the table): ip5 and ip12. In both cases the analysis detected "children" of the injected signal, with parameters significantly different from those of the injection. Injection ip11 has been discarded in the last stage of the follow-up because it did not pass the CR consistency veto among single detectors, although its parameters are recovered with good accuracy.

Label	CR	Frequency [Hz]	Spin-down [nHz/s]	α [deg]	δ [deg]
ip10	37.9	26.34211 (0.00019)	−0.0671 (0.0179)	219.6584(−1.896)	43.6464 (0.769)
ip11	118.5	31.42512 (0.00027)	−0.0742 (−0.0736)	274.4572(−10.640)	−49.2362 (9.033)
ip3	87.8	108.85705(−0.00011)	0.01645 (0.0164)	177.5770(−0.795)	−34.1960 (−0.759)
ip6	42.2	146.16382(−0.00045)	−6.7099 (0.0201)	358.6904(−0.061)	−65.2405 (0.182)
ip8	138.6	191.02390(−0.00013)	−8.7161 (−0.0661)	351.2037(−0.186)	−35.0975 (−1.679)
ip0	180.7	265.57572 (0.00019)	−0.0483 (−0.0441)	73.0276 (1.476)	−57.0156 (−0.798)

TABLE VI. *SkyHough* hardware injection cluster information. The table provides the frequency, spin-down and sky location of the cluster center related to each of the hardware injections found by the *SkyHough* search. In parentheses the absolute errors with respect to the injected values are shown. Frequencies are converted to epoch GPS 1125972653.

Label	s_{mean}	Frequency [Hz]	Spin-down [nHz/s]	α [deg]	δ [deg]
ip5	24.22	52.8084 (0.0001)	−0.0175 (0.0175)	294.2376 (8.3890)	−83.1460 (0.6932)
ip3	13.61	108.8573 (0.0002)	0.0041 (0.0041)	179.7435 (1.3709)	−32.7633 (0.6733)
ip6	16.08	146.1994 (0.0006)	−6.6167 (0.1133)	362.8627 (1.6137)	−63.7860 (1.6367)
ip8	22.83	191.0716 (0.0009)	−8.7553 (0.1053)	348.0175 (3.3721)	−31.7070 (1.7115)
ip0	21.16	265.5736 (0.0020)	0.3441 (0.3482)	68.7247 (2.8272)	−52.1531 (4.0643)

been computed in each 0.1-Hz band, except for the 194 bands in which outliers were found.

E. *Time-Domain $\mathcal{F}$-statistic* search results

In the bandwidth searched [10, 475] Hz, 1921 0.25-Hz long bands were defined [see Eq. (13)]. As a result of vetoing candidates around the known interference lines, a certain fraction of the bandwidth was not analyzed. In Fig. 19 we show the fraction of the bandwidth vetoed for each band. As a result, 22% of the [10, 475] Hz band was vetoed, overall.

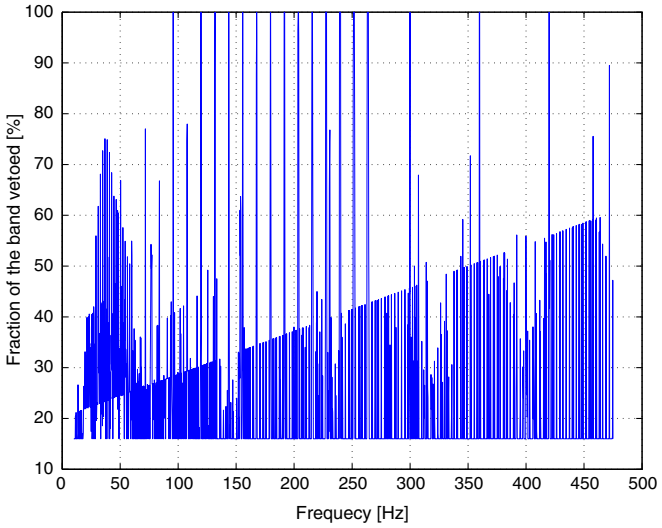

FIG. 19. Fraction of the bandwidth vetoed for each band searched by the *Time-Domain $\mathcal{F}$-statistic* pipeline.

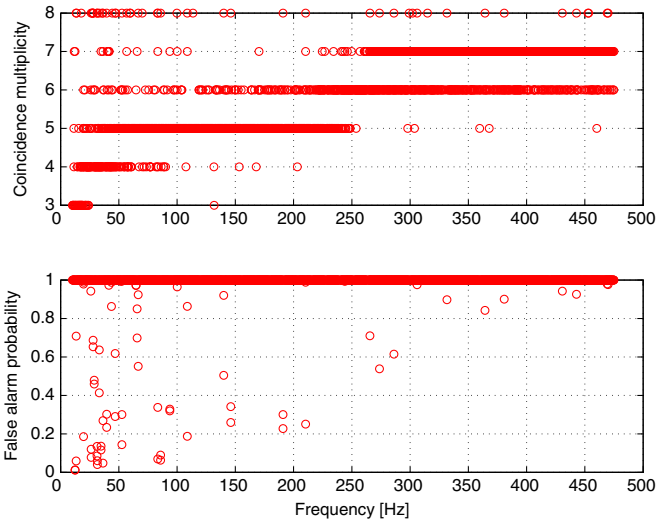

FIG. 20. *Time-Domain $\mathcal{F}$-statistic* pipeline coincidence results as a function of the band frequency. Top panel: maximum coincidence multiplicity. Bottom panel: false alarm probability for the coincidence with the maximum multiplicity.

TABLE VII. Hardware injection recovery with the *Time-Domain $\mathcal{F}$-statistic* pipeline. The values in parentheses are the absolute errors, that is, the difference with respect to the injection parameters. Frequencies are converted to epoch GPS 1130737464.

Label	FA	Frequency [Hz]	Spin-down [nHz/s]	α [deg]	δ [deg]
ip0	70	265.57565(−0.00012)	0.2582(−0.2602)	68.6196 (2.932)	−53.7294 (−2.488)
ip3	19	108.85713(−0.00003)	0.0158 (0.0158)	172.0773 (6.295)	−30.6495 (−2.787)
ip5	30	52.8085(−0.00015)	−0.2168 (0.2168)	273.6538 (28.972)	−63.6095 (−20.230)
ip6	34	146.16861(−0.00064)	−6.8469 (0.1169)	350.4083 (8.343)	−64.2301 (−1.192)
ip8	23	191.02942 (0.00004)	−8.2475 (−0.4024)	340.2146 (11.175)	8.6891(−42.108)
ip10	55	26.34206(−0.00016)	−0.0763 (0.0087)	226.9401(−5.384)	41.1968 (1.680)
ip11	89	31.42490(−0.00014)	−0.0798 (−0.803)	301.7315(−16.634)	−53.2623 (5.010)

Of 1921 bands analyzed, 38 bands were completely vetoed because of line artifacts. As a result of the coherent search in 15368 data segments, we obtained around 6.2×10^{11} candidates. These candidates were subject to a search for initial coincidences in a second stage of the *Time-Domain $\mathcal{F}$-statistic* analysis. The search for coincidences was performed in all the bands except for the above-mentioned 38 that were completely vetoed. Also, in addition to the 38 bands vetoed because of line artifacts, there were 13 highly disturbed bands for which no coincidence results were obtained because there were too many candidates for the current coincidence program to handle properly. In the coincidence analysis, for each band, the coincidences among the candidates were searched in eight 6-day-long time frames. In Fig. 20 the results of the coincidence search are presented. The top panel shows the maximum coincidence multiplicity for each of the bands analyzed. The maximum multiplicity is an integer that varies from 3 to 8 because we require coincidence multiplicity of at least 3, and 8 is the number of time frames analyzed.

The bottom panel of Fig. 20 shows the results for the false alarm probability of coincidence for the coincidence with the maximum multiplicity. This false alarm probability is calculated using the formula from the appendix of [19].

For further analysis 49 coincidences with the lowest false alarm probability were selected. The parameters of these coincidences are listed in Table XIII in Appendix D: they are the outliers of the search. The parameters of a given

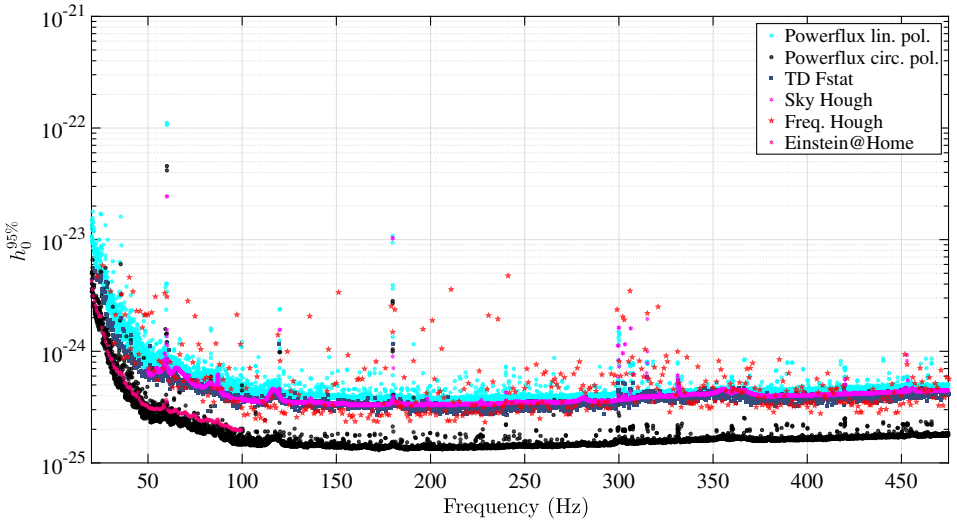

FIG. 21. Upper limit comparison for the four search pipelines used in this analysis. The curves represent the source strain amplitude h_0 at which 95% of simulated signals would be detected. Three of the pipelines (*FrequencyHough*, *SkyHough*, *Time-Domain $\mathcal{F}$-statistic*) present population-averaged limits over the full sky and source polarization, while one pipeline (*PowerFlux*) presents strict all-sky limits for circular-polarization (most favorable orientation: black) and linear-polarization (least favorable orientation: cyan) sources. Converting the *PowerFlux* upper limits to validated population-averaged upper limits would require extensive, band-dependent Monte Carlo simulations, but previous studies suggest that such limits would lie in a region similar to that of the other pipelines. In addition, the population-averaged upper limits from the most recent Einstein@Home search are shown for comparison [32]. The Einstein@Home search explored the low frequencies, and a narrower spin-down range using a much longer coherence length (210 hours).

coincidence are calculated as the mean values of the parameters of the candidates that enter a given coincidence. Among these 49 outliers, 11 are identified with the hardware injections. Table VII presents the estimated parameters obtained for these hardware injections, along with the absolute errors of the reconstructed parameters (the differences with respect to the injected parameters). The remaining 38 outliers include 6 associated with the 0.25-Hz comb, 15 seen in only one interferometer, 4 in only the first half of the run, 1 transient disturbance, 8 corresponding to *PowerFlux* outliers already excluded and 2 (numbers 10 and 11) requiring further, deep follow-up (although inconsistent structures seen in run-averaged H1 and L1 spectra in that band already cast doubt on an astrophysical origin). The deep follow-up used the same method [31,32] as for persistent outliers in the other search pipelines. Again, no credible signals were found.

VI. CONCLUSIONS

We have performed the most sensitive all-sky searches to date for continuous gravitational waves in the range 20–475 Hz, using four independent search programs that apply a variety of algorithmic approaches with different parameter choices and different approaches to handling instrumental contaminations. The overall improvements in strain sensitivity come primarily from the improved noise floors of the Advanced LIGO interferometers over previous LIGO and Virgo interferometers, with reductions in upper limits of about a factor of 3 at frequencies above 100 Hz and larger reductions at lower frequencies. We explored both positive and negative spin-downs and found no credible gravitational wave signals, allowing upper limits to be placed on possible source signal amplitudes. Fig. 21 shows a summary of the strain amplitude upper limits obtained for the four pipelines. Three of the pipelines (*FrequencyHough*, *SkyHough*, *Time-Domain $\mathcal{F}$-statistic*) present population-averaged limits over the full sky and source polarization, while one pipeline (*PowerFlux*) presents strict all-sky limits for circular-polarization and linear-polarization sources.

At the highest frequencies we are sensitive to neutron stars with an equatorial ellipticity as small as 8×10^{-7} and as far away as 1 kpc for favorable spin orientations. The maximum ellipticity a neutron star can theoretically support is at least 1×10^{-5} according to [50,51]. Our results exclude such maximally deformed pulsars above 200 Hz pulsar rotation frequency (400 Hz gravitational frequency) within 1 kpc. Outliers from initial stages of each search method were followed up systematically, but no candidates from any search survived scrutiny.

ACKNOWLEDGMENTS

The authors gratefully acknowledge the support of the United States National Science Foundation (NSF) for the construction and operation of the LIGO Laboratory and Advanced LIGO as well as the Science and Technology Facilities Council (STFC) of the United Kingdom, the Max-Planck-Society (MPS), and the State of Niedersachsen/Germany for support of the construction of Advanced LIGO and construction and operation of the GEO600 detector. Additional support for Advanced LIGO was provided by the Australian Research Council. The authors gratefully acknowledge the Italian Istituto Nazionale di Fisica Nucleare (INFN), the French Centre National de la Recherche Scientifique (CNRS) and the Foundation for Fundamental Research on Matter supported by the Netherlands Organisation for Scientific Research, for the construction and operation of the Virgo detector and the creation and support of the EGO consortium. The authors also gratefully acknowledge research support from these agencies as well as by the Council of Scientific and Industrial Research of India; Department of Science and Technology, India; Science & Engineering Research Board (SERB), India; Ministry of Human Resource Development, India; the Spanish Ministerio de Economía y Competitividad; the Vicepresidència i Conselleria d'Innovació; Recerca i Turisme and the Conselleria d'Educació i Universitat del Govern de les Illes Balears; the National Science Centre of Poland; the European Commission; the Royal Society; the Scottish Funding Council; the Scottish Universities Physics Alliance; the Hungarian Scientific Research Fund (OTKA); the Lyon Institute of Origins (LIO); the National Research Foundation of Korea; Industry Canada and the Province of Ontario through the Ministry of Economic Development and Innovation; the Natural Science and Engineering Research Council Canada; Canadian Institute for Advanced Research; the Brazilian Ministry of Science, Technology, and Innovation; International Center for Theoretical Physics South American Institute for Fundamental Research (ICTP-SAIFR); Russian Foundation for Basic Research; the Leverhulme Trust; the Research Corporation,; Ministry of Science and Technology (MOST), Taiwan and the Kavli Foundation. The authors gratefully acknowledge the support of the NSF, STFC, MPS, INFN, CNRS, PL-Grid and the State of Niedersachsen/Germany for provision of computational resources. This document has been assigned LIGO Laboratory document No. `LIGO-P1700052-v18`.

APPENDIX A: *POWERFLUX* OUTLIER TABLES

PowerFlux outliers are separated into three categories. Of the most interest are outliers in Table VIII spanning two or more segments that are outside a known comb of 0.25 Hz lines. Outliers spanning only one segment are presented in Table IX. Finally, Table X lists outliers near 0.25 Hz comb.

TABLE VIII. Outliers that passed *PowerFlux* detection pipeline spanning more than one segment and excluding those near a 0.25-Hz comb. Only the highest-SNR outlier is shown for each 0.1-Hz frequency region. Outliers marked with "line" had strong narrowband disturbances identified near the outlier location. The "Segment" column reports the set of contiguous segments of the data that produced the outlier, as described in Sec. V. Frequencies are converted to epoch GPS 1130529362.

Idx	SNR	Segment	Frequency Hz	Spin-down nHz/s	RA_{J2000} degrees	DEC_{J2000} degrees	Description
1	10532	[0, 2]	256.00854	−1.475	255.225	−85.537	Extremely strong bin-centered line at 256.0 Hz
33	352	[1, 2]	52.80829	0.000	301.148	−84.274	Hardware injection ip5
36	269	[0, 2]	191.03127	−8.663	351.292	−33.643	Hardware injection ip8
37	236	[1, 2]	265.57551	−0.013	71.719	−56.276	Hardware injection ip0
39	227	[0, 1]	21.41061	−0.500	230.715	−1.630	Sharp line in L1 near 21.41 Hz, H1 and L1 SNR inconsistent
46	172	[1, 2]	146.16942	−6.775	356.992	−65.953	Hardware injection ip6
47	170	[0, 1]	31.11704	−7.362	56.406	−22.568	Coincident combs with different morphology between H1 and L1
52	145	[1, 2]	108.85708	0.037	176.861	−34.170	Hardware injection ip3
56	110	[0, 1]	59.60507	0.113	283.407	68.377	Coincident lines in spectrum, signal nearly stationary in detector frame
70	63	[1, 2]	99.96961	1.775	99.689	35.244	Coincident regions between H1 and L1
72	52	[1, 2]	30.63391	−6.688	357.777	−40.140	Both H1 and L1 spectra are contaminated
74	48	[1, 2]	412.00362	−0.588	84.695	−71.077	Sharp bin-centered line in L1 at 412.0 Hz
78	39	[0, 1]	93.75912	0.062	279.035	−13.320	Sharp and coincident lines in H1 and L1, SNR inconsistent
85	33	[0, 1]	299.42508	1.175	317.303	46.331	All SNR comes from large artifact in H1
95	23	[0, 2]	90.74396	0.250	86.019	−18.203	Coincident bin-centered lines at 90.75 Hz, 0.25 Hz comb
98	19	[0, 2]	33.59221	0.300	359.165	−18.874	Both H1 and L1 spectra are disturbed, H1 does not see anything
99	19	[1, 2]	306.01509	−2.275	130.248	33.827	Large artifact in L1, H1 does not see anything
100	19	[0, 2]	299.39436	−0.287	116.867	73.521	Large artifact in H1, L1 does not see anything
102	17	[0, 2]	307.31880	−6.612	181.054	−25.115	Large artifact in L1, H1 does not see anything
109	16	[0, 1]	452.88717	0.238	82.204	−67.295	Large artifact in H1
122	14	[1, 2]	452.86305	−2.350	198.764	49.143	Large artifact in H1
128	13	[1, 2]	29.63552	0.312	107.619	1.373	Coincident disturbances with different morphologies in H1 and L1
134	13	[1, 2]	265.75911	−2.112	67.964	−28.799	Not confirmed by Einstein@Home followup
138	13	[0, 1]	178.60606	−3.275	194.163	51.285	Sharp line in L1 at 178.7 Hz is outside signal range
154	12	[1, 2]	404.79214	−6.675	136.431	38.381	Not confirmed by Einstein@Home followup

TABLE IX. Outliers that passed *PowerFlux* detection pipeline spanning only one segment, excluding those near 0.25-Hz comb. Only the highest-SNR outlier is shown for each 0.1-Hz frequency region. Outliers marked with "line" had strong narrowband disturbances identified near the outlier location. Segment column reports the set of contiguous segments of the data that produced the outlier, as described in Sec. V. Frequencies are converted to epoch GPS 1130529362.

Idx	SNR	Segment	Frequency Hz	Spin-down nHz/s	RA_{J2000} degrees	DEC_{J2000} degrees	Description
3	5470	[1, 1]	35.70737	−0.287	71.099	−89.596	Broadly coincident region between 35.7 and 35.71
22	933	[2, 2]	35.76455	−0.700	241.377	−7.873	Broadly coincident region
31	417	[1, 1]	59.51547	−2.112	282.450	16.555	Coincident regions
40	223	[1, 1]	83.31080	−2.000	184.935	−16.484	Coincident regions between H1 and L1
41	197	[0, 0]	100.00749	0.650	319.773	−59.068	Coincident regions between H1 and L1
43	185	[0, 0]	113.68611	1.062	26.888	−57.341	Strong line in H1, H1 and L1 SNR inconsistent

(Table continued)

TABLE IX. *(Continued)*

Idx	SNR	Segment	Frequency Hz	Spin-down nHz/s	RA_{J2000} degrees	DEC_{J2000} degrees	Description
45	177	[2, 2]	31.42488	−0.062	278.446	−49.515	Coincident regions between H1 and L1, is this really an injection
48	163	[2, 2]	46.95114	−0.350	132.597	−88.847	Coincident sharp lines at 46.95
49	152	[2, 2]	38.47802	−6.312	326.542	−17.113	Hardware injection ip12
57	108	[2, 2]	440.50273	1.762	65.270	−37.191	Sharp line in L1 at 440.5
62	86	[0, 0]	40.87517	0.375	236.742	79.741	Elevated and disturbed spectrum, uneven sensitivity during run
66	70	[1, 1]	31.76233	0.613	64.921	−9.503	Coincident lines in H1 and L1
77	39	[1, 1]	39.76505	−0.250	298.570	42.651	Sharp and coincident lines in H1 and L1
82	37	[2, 2]	78.50513	−0.688	299.793	45.680	Sharp and coincident lines at 78.5 Hz, 0.25 Hz comb
83	34	[2, 2]	128.49647	0.962	323.700	86.937	Outlier favors region next to the line at 128.5 Hz
87	32	[1, 1]	32.60162	−0.912	221.578	10.228	All SNR comes from disturbance in L1
89	29	[2, 2]	127.50310	−0.900	135.660	−85.458	Coincident bin-centered lines at 127.5 Hz in both ifos
90	28	[1, 1]	47.68505	−4.125	80.941	−75.614	H1 and L1 disagree on location, common overlapping artifact
92	24	[0, 0]	246.30806	−0.800	257.315	−88.956	Coincident bin-centered lines at 246.3 Hz
96	22	[0, 0]	453.38509	−7.400	213.641	21.911	Large artifact in H1, L1 does not see anything
97	22	[0, 0]	70.92119	0.275	136.639	−68.924	Coincident artifacts in H1 and L1
101	17	[0, 0]	306.00102	−6.513	106.860	−14.138	Small disturbance in L1
104	17	[2, 2]	26.36415	−9.013	62.782	−13.429	Coincident combs, large artifact with different morphology in H1 and L1
105	16	[1, 1]	43.68056	0.087	114.317	−3.107	Large artifact in L1
106	16	[0, 0]	327.59196	−8.162	23.524	−50.419	
107	16	[1, 1]	31.61544	0.238	17.372	−10.319	Different disturbances in H1 and L1 spectrum
108	16	[0, 0]	308.99815	−3.925	289.216	47.738	
110	15	[1, 1]	337.31874	−0.675	244.827	41.178	
111	15	[0, 0]	350.25984	−8.188	313.477	−34.804	
112	15	[0, 0]	345.08507	0.900	136.135	40.606	
113	15	[0, 0]	453.35293	−5.725	143.703	64.705	Appears to be associated with artifact at 453.40 Hz
114	14	[0, 0]	254.15359	−9.938	204.993	43.892	Weak sharp line in L1 at 241.1 Hz
115	14	[0, 0]	436.09611	−6.750	346.514	−36.245	
116	14	[0, 0]	310.92629	−3.975	359.968	14.226	
117	14	[1, 1]	162.18514	−1.587	101.520	−3.877	
118	14	[2, 2]	454.18958	−4.138	254.665	0.668	Sharp line in L1 at 454 Hz is outside signal range
119	14	[1, 1]	225.64096	−2.725	234.719	31.199	Large artifact in H1
120	14	[0, 0]	394.54298	−2.238	147.069	51.380	
121	14	[1, 1]	270.50488	1.025	192.977	26.380	Sharp line in L1 at 270.5 is outside signal range
123	14	[2, 2]	213.68406	0.413	203.168	36.792	
124	14	[1, 1]	293.36763	−0.725	291.910	−39.555	
125	13	[1, 1]	336.94860	−1.212	29.971	−40.200	
126	13	[1, 1]	318.76465	−7.375	203.369	39.161	Sharp line in L1 at 318.80 Hz is outside signal range
127	13	[1, 1]	97.00786	−4.338	152.289	42.607	Sharp line in L1 at 97.1 Hz is outside signal range
129	13	[2, 2]	446.76910	−5.237	275.842	27.684	
130	13	[2, 2]	415.31493	−0.625	246.343	35.521	Sharp line in L1 at 415.4 Hz is outside signal range
131	13	[1, 1]	289.16717	−4.812	289.555	56.661	Sharp line in L1 at 289.3 Hz is outside signal range
132	13	[2, 2]	435.04082	1.175	61.748	−49.375	
133	13	[0, 0]	353.38444	−7.325	267.522	65.417	
135	13	[0, 0]	247.50050	−5.975	60.313	−25.256	Sharp line in L1 at 247.3 is outside signal range
136	13	[0, 0]	463.10329	−1.700	30.527	−20.284	Sharp line in L1 at 463.2 Hz is outside signal range
137	13	[1, 1]	380.57045	−9.338	244.202	45.262	Sharp line in L1 at 480.6 Hz is outside signal range
139	13	[2, 2]	443.65961	−1.988	82.034	−43.630	
140	13	[1, 1]	442.16364	−6.525	80.319	31.835	
141	13	[2, 2]	437.40225	−9.825	139.879	−37.221	Lines in H1 and L1 outside signal range

(Table continued)

TABLE IX. *(Continued)*

Idx	SNR	Segment	Frequency Hz	Spin-down nHz/s	RA_{J2000} degrees	DEC_{J2000} degrees	Description
142	13	[1, 1]	474.28332	−8.562	354.078	39.661	Sharp line in L1 at 474.3
143	13	[0, 0]	232.64393	−7.500	244.442	30.182	Sharp line in L1 at 232.8
144	13	[2, 2]	455.60513	−9.125	264.100	12.723	Identical slope in H1 and L1 spectrum
145	13	[2, 2]	321.96324	−5.425	88.612	−18.667	Disturbed H1 spectrum
146	13	[0, 0]	377.36117	−3.900	162.703	19.347	
147	13	[1, 1]	463.81555	−2.762	92.427	−21.270	Sharp line in L1 at 463.7 is outside signal range
148	12	[2, 2]	369.43296	1.113	318.118	43.385	Sharp line in L1 at 369.5 is outside signal range
149	12	[0, 0]	348.24255	−2.862	249.590	53.903	Sharp line in L1 at 348.2 is outside signal range
150	12	[1, 1]	293.17864	−1.713	1.204	9.380	
151	12	[1, 1]	371.37093	−9.562	17.812	−38.934	
152	12	[2, 2]	418.80178	−9.588	180.042	−37.122	
153	12	[0, 0]	56.38793	0.812	11.265	−26.818	Rather large disturbance in L1 outside signal range
155	12	[1, 1]	389.58663	0.375	190.109	39.234	
156	12	[1, 1]	381.17708	−8.162	327.725	−27.100	Sharp line in L1 at 381.1 is outside signal range
157	12	[1, 1]	471.92300	0.800	351.848	−37.756	Sharp line in H1 at 472 Hz, sharp line in L1 471.9 Hz
158	12	[0, 0]	231.41586	−6.038	151.842	51.699	
159	12	[1, 1]	384.21151	−5.938	205.820	36.442	Sharp line in H1 at 384 Hz is far outside signal range
160	12	[2, 2]	359.81255	−0.875	278.065	26.246	Outlier favors sidelobes of 60 Hz harmonic
161	12	[0, 0]	302.90153	0.150	323.285	−57.949	

TABLE X. *PowerFlux* outliers below 100 Hz found within 5 mHz of 0.25-Hz comb. Only the highest-SNR outlier is shown for each 0.1-Hz frequency region. Segment column reports the set of contiguous segments of the data that produced the outlier, as described in Sec. V. Frequencies are converted to epoch GPS 1130529362.

Idx	SNR	Segment	Frequency Hz	Spin-down nHz/s	RA_{J2000} degrees	DEC_{J2000} degrees
2	5603	[1, 2]	21.50025	−0.150	151.422	−79.107
4	4996	[1, 2]	34.49925	0.350	21.714	77.506
5	4938	[0, 2]	25.00029	−0.413	234.953	13.114
7	4207	[0, 2]	29.50008	−0.150	131.116	−74.570
10	2921	[1, 2]	20.49974	0.113	309.323	79.014
11	2721	[0, 2]	33.24851	−0.050	196.925	82.946
15	1593	[0, 2]	47.49882	0.463	23.877	80.095
17	1493	[1, 2]	46.49823	0.725	55.515	60.238
18	1238	[0, 1]	23.24905	0.263	62.224	5.482
19	1161	[0, 2]	31.25038	−0.137	156.015	−78.649
23	914	[0, 2]	54.50016	0.275	311.453	70.504
25	837	[0, 2]	22.24910	−0.413	201.320	17.588
27	615	[0, 2]	58.50283	−0.575	293.833	−81.976
28	587	[0, 2]	57.49720	1.012	65.281	51.741
29	551	[0, 2]	41.50357	−0.450	314.469	−57.748
30	421	[0, 2]	43.24808	−0.062	221.374	82.111
35	305	[0, 1]	48.24916	−0.200	246.369	59.628
38	229	[0, 2]	20.24852	0.025	94.536	−6.808
44	179	[0, 1]	27.24799	−1.475	248.015	−15.916
50	151	[0, 2]	50.24710	−0.037	134.356	86.279
53	141	[1, 2]	42.99932	0.325	341.196	79.984
54	140	[1, 2]	34.24893	0.450	43.246	68.520
59	106	[0, 1]	66.75438	0.175	29.149	89.424
60	98	[0, 2]	38.99998	−0.025	94.142	−67.898

(Table continued)

TABLE X. *(Continued)*

Idx	SNR	Segment	Frequency Hz	Spin-down nHz/s	RA_{J2000} degrees	DEC_{J2000} degrees
63	85	[0, 1]	85.50355	−0.537	285.886	−82.302
64	79	[1, 2]	40.00031	−0.175	115.403	−76.647
65	76	[0, 2]	45.00071	0.062	17.453	−83.230
67	68	[1, 2]	39.25073	−0.525	215.636	−65.846
68	66	[0, 2]	98.49708	0.750	330.835	87.908
76	44	[1, 2]	21.24994	−0.037	255.942	63.243
86	32	[0, 2]	88.75324	−0.062	212.757	−88.557
91	25	[0, 2]	89.75337	0.775	317.050	51.127
93	24	[0, 2]	91.75467	−0.338	260.215	23.279
103	17	[0, 2]	97.75447	−1.075	245.495	−8.107
6	4508	[2, 2]	23.50090	−0.250	240.850	−80.885
8	3346	[2, 2]	42.49877	0.400	30.333	83.056
9	3071	[1, 1]	28.49919	0.250	35.734	80.126
12	2269	[2, 2]	36.50033	0.200	329.266	68.973
13	2218	[0, 0]	30.50049	0.062	66.712	−70.484
14	1864	[0, 0]	33.49977	0.025	272.862	72.497
16	1581	[1, 1]	24.50010	0.163	327.225	69.131
20	1155	[1, 1]	31.49812	−0.150	183.141	56.041
21	1112	[1, 1]	39.50029	−0.400	182.468	−69.888
24	881	[0, 0]	37.50214	0.050	308.365	−78.677
26	652	[0, 0]	48.50039	0.087	283.523	66.911
32	414	[0, 0]	25.24979	0.312	48.291	−15.967
34	339	[0, 0]	25.49812	−0.200	163.735	61.435
42	194	[2, 2]	71.50111	−0.438	261.002	49.485
51	148	[2, 2]	26.25072	−0.275	212.451	−78.398
55	122	[0, 0]	60.50055	0.087	281.309	63.866
58	107	[1, 1]	31.99943	0.250	6.435	78.791
61	97	[1, 1]	30.00010	−0.200	147.604	−74.370
69	65	[0, 0]	30.99823	0.087	76.765	69.482
71	57	[2, 2]	84.99812	0.525	292.900	84.017
73	52	[1, 1]	37.25095	−0.338	218.785	−80.271
75	44	[2, 2]	57.00140	−0.463	175.217	−84.532
79	39	[2, 2]	46.25171	−0.713	240.550	−62.392
80	38	[2, 2]	44.25014	−0.250	132.213	−77.498
81	37	[2, 2]	38.00200	−0.762	250.147	−18.662
84	33	[1, 1]	36.25184	−0.400	270.188	−69.467
88	31	[1, 1]	50.00082	−0.325	148.358	−81.767
94	23	[2, 2]	41.24653	−0.100	150.901	−22.875

APPENDIX B: *FREQUENCYHOUGH* OUTLIER TABLES

In this section we describe in some detail the final outliers found in the *FrequencyHough* search and the analyses that have been carried on them. Table XI contains the list of the outliers and their main characteristic, including a brief comment. Each of these outliers has been manually examined by looking at the details of the follow-up products, including the peakmaps and the Hough maps, and comparing single detector and joint results. For all of these outliers a gravitational wave origin can be excluded. For outliers 2–5 and 10 in Table XI, the presence of instrumental artifacts (of unknown origin) is clear. Outliers 1, 6, 8, 11 and 13 are not consistent between the two detectors. In particular, outliers 8 and 11 are attributed to transient disturbance in the Hanford detector. Outlier 9 is consistent between detectors, but not highly significant in the two detectors. Finally, outliers 7, 12 and 14 were potentially more interesting: they are consistent among the two detectors, very significant also in the single-interferometer analysis and the corresponding Hough maps look reasonable. As an example, in Fig. 22 we plot the corrected peakmap projections for outlier 7, and in Fig. 23 the outlier joint Hough map. For these outliers we have carried out a deeper follow-up using the method described in [31,32], with a coherence time of 210 hours. In all cases the follow-up failed to yield a credible signal. Hence, none of the above outliers shows evidence of a true gravitational wave signal.

TABLE XI. Final outliers selected by the *FrequencyHough* pipeline. Each of them is identified by the frequency, the spin-down, the position in equatorial coordinates and the critical ratio computed on the corrected peakmap projection. Reference time is MJD = 57328.59684 (GPS 1130509183.976).

Idx	Frequency [Hz]	Spin-down [Hz/s]	α [deg]	δ [deg]	CR	Description
1	19.3245	-9.2235×10^{-9}	210.16	−20.47	12.9	Due to H1 alone
2	27.8422	-8.2416×10^{-11}	123.54	−70.26	41.7	Instrumental artifact mainly in L1
3	27.8425	-7.1820×10^{-11}	76.67	−74.73	63.2	Instrumental artifact mainly in L1
4	59.6054	-7.8884×10^{-11}	98.17	−70.46	51.2	Two nearby instrumental artifacts in H1 and L1
5	59.6053	-8.2416×10^{-11}	263.16	62.68	39.9	Two nearby instrumental artifacts in H1 and L1
6	217.4516	$+1.8249 \times 10^{-10}$	77.15	−31.98	7.8	Due to H1 alone
7	231.6987	-1.4128×10^{-9}	288.08	36.63	9.0	Consistent among H1 and L1
8	269.8699	-5.7679×10^{-9}	242.98	33.60	7.9	Possibly transient disturbance in H1
9	281.5976	-2.5184×10^{-9}	166.49	44.47	7.8	Consistent but not highly significant in single IFOs
10	289.8485	-6.9783×10^{-9}	276.08	32.80	9.8	Instrumental artifact in L1
11	294.5292	-1.1774×10^{-10}	316.32	30.28	7.9	Possibly transient disturbance in H1
12	304.8360	-5.1687×10^{-10}	74.14	−41.39	7.6	Consistent among H1 and L1
13	393.3830	-7.2997×10^{-10}	37.59	−24.43	7.7	Not consistent among single IFOs
14	456.9495	-3.0612×10^{-10}	248.33	44.97	8.0	Consistent among H1 and L1

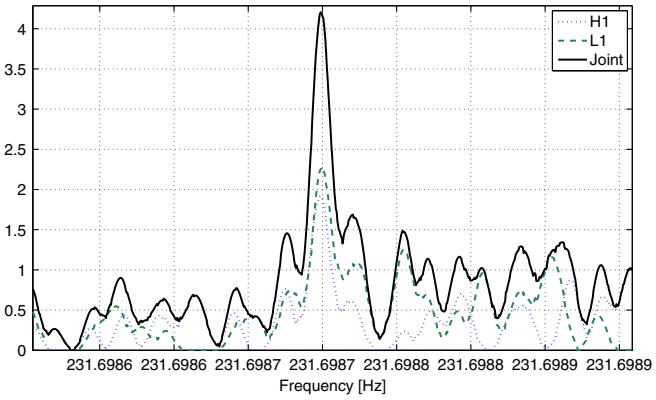

FIG. 22. Peakmap projections for outlier 7 of the *FrequencyHough* search. The dotted blue line is for Hanford detector analysis, the green dashed line is for Livingston detector analysis and the continuous black line is for the joint search.

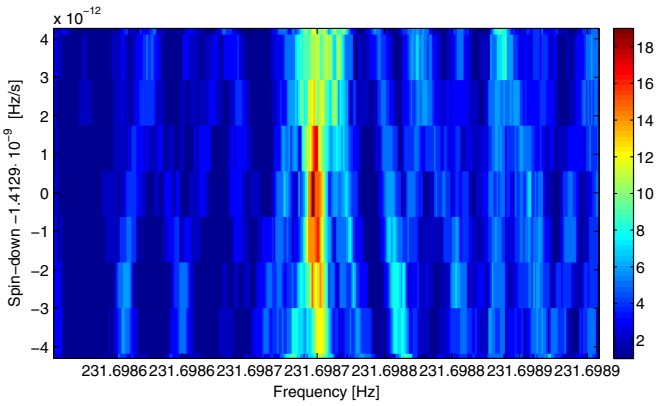

FIG. 23. Joint Hough map for outlier 7 of the *FrequencyHough* search.

APPENDIX C: *SKYHOUGH* OUTLIER TABLES

Table XII presents the parameters of the final 26 outliers from the *SkyHough* search pipeline, along with comments on their likely causes. None is a credible gravitational wave signal.

TABLE XII. *SkyHough* outliers after population and multi-interferometer consistency vetoes. The table provides the frequency, spin-down and sky location of the cluster centers found by the *SkyHough* search. $\#_{\text{cluster}}$ is the size of the cluster in terms of number of coincident pairs, $s_{\max}$ and s_{mean} are the maximum and mean values of the cluster significance, $\#_{L1}$ and $\#_{H1}$ are the number of different candidates producing coincidence pairs from the different data sets, s^*_{L1} and s^*_{H1} are the maximum significance values obtained by analyzing the data from H1 and L1 separately, s^*_{multi} is maximum combined significance when the data from both detectors are analyzed jointly and s_{theo} is the expected theoretical combined significance value. Frequencies are converted to epoch GPS 1125972653. The outlier description codes mean the following: 1—hardware injection, 2—associated to unknown comb in H1 starting at 30.9430 Hz with 0.99816 Hz spacing, 3—miscellaneous combs with known or unknown sources at multiples of 0.5 Hz many of them due to blinking LEDs in timing system, 4—associated with the 8-Hz comb in H1 due to the OMC length dither, and 5-spectral disturbance in H1.

Idx	Frequency [Hz]	Spin-down [nHz/s]	α [rad]	δ [rad]	s_{mean}	$\#_{\text{cluster}}$	$\#_{\text{L1}}$	$\#_{\text{H1}}$	s^*_{L1}	s^*_{H1}	$s_{\max}$	s^*_{multi}	s_{theo}	Description
6	52.8084	−0.0175	−1.1478	−1.4512	24.22	975	554	20	20.36	40.54	27.02	45.61	45.20	1
9	53.8974	0.3693	0.4803	1.5115	6.31	14	6	3	5.66	10.47	6.50	21.20	11.90	2
14	57.0055	−1.0014	−2.2336	−0.1685	9.84	14	7	2	15.84	9.17	11.43	14.28	15.37	3
24	62.4983	0.2480	−1.0927	1.3699	14.64	1089	45	326	9.13	98.01	16.67	95.25	93.06	3
44	75.5055	−0.9098	−2.5598	−1.1455	10.05	7	2	5	6.44	71.67	11.67	57.12	57.60	3
46	76.4988	0.2207	−1.1572	1.2721	11.03	1090	34	282	7.59	76.60	11.49	68.14	67.41	3
47	77.4963	0.5741	−0.1180	1.3766	9.54	959	70	121	6.28	76.87	10.61	70.23	66.58	3
49	78.4962	0.5587	−0.2021	1.4096	9.65	308	13	129	6.38	75.89	10.29	69.25	64.34	3
52	79.9990	0.1808	−1.2674	1.2599	10.05	615	59	175	6.59	107.63	10.90	97.21	91.77	3, 4
53	80.4994	0.0658	−1.5722	1.2107	11.92	1254	97	138	7.41	68.79	13.27	60.94	60.89	3
60	84.4961	0.5454	−0.4443	1.4369	8.95	1002	55	141	5.88	59.19	10.69	56.18	54.21	3
62	85.0013	−0.2165	1.8264	−1.2866	12.08	811	132	83	11.21	15.38	12.96	18.13	18.96	3
63	85.5012	−0.1977	1.7877	−1.2674	33.87	870	198	64	27.44	58.03	36.95	63.92	63.78	3
66	86.4989	0.1618	−1.4494	1.2580	9.08	1357	147	125	6.38	57.24	10.49	54.70	53.67	3
76	98.4983	0.2876	−1.2383	1.2866	10.16	1219	161	158	7.10	28.50	11.30	27.51	26.12	3
79	100.5032	−0.5624	2.5925	−1.3402	8.37	288	39	114	6.02	28	8.85	24.96	24.96	3
88	108.8573	0.0041	−3.1371	−0.5718	13.61	999	296	99	18.79	14.73	15.85	22.93	23.55	1
92	112.5026	−0.4739	−1.8331	0.9775	6.52	68	2	55	5.98	11.70	6.78	11.72	12.84	3
104	127.4964	0.5926	−0.9377	1.3368	6.36	877	204	58	7.04	7.64	6.94	9.08	10.39	3
105	127.9988	0.2101	−1.3924	1.2317	70.70	1165	161	70	61.13	108	78.07	123.85	121.24	3, 4
107	128.4984	0.3602	−1.1366	1.2478	6.94	971	223	82	8.40	7.35	7.60	9.50	11.07	3
112	146.1994	−6.6167	0.0500	−1.1133	16.08	1676	796	22	15.96	22.10	18.11	27.17	26.87	1
136	191.0716	−8.7553	−0.2091	−0.5534	22.83	988	262	107	30.61	22.80	25.66	37.00	37.76	1
153	255.9995	0.0789	−1.5493	1.1792	30.62	1082	203	43	20.10	105.72	33.03	96.46	86.90	3, 4
160	265.5736	0.3441	1.1995	−0.9102	21.16	750	286	18	24.76	25.97	25.19	35.18	35.85	1
193	452.8999	−2.7816	2.5350	−1.3173	10.01	222	4	109	6.68	88.07	10.04	61.91	28.21	5

APPENDIX D: *TIME-DOMAIN $\mathcal{F}$-STATISTIC* OUTLIER TABLES

Table XIII presents the parameters of the final 49 outliers from the *Time-Domain $\mathcal{F}$-statistic* pipeline, along with comments on their likely causes. None is a credible gravitational wave signal.

TABLE XIII. *Time-Domain $\mathcal{F}$-statistic* pipeline outliers in the range of frequencies between 10 and 475 Hz. The columns provide the nominal frequencies and frequency derivatives, right ascensions and declinations found for the outliers, along with comments indicating the likely sources of the outliers.

Idx	Frequency Hz	Spin-down nHz/s	RA_{J2000} degrees	$\text{DEC}_{\text{J2000}}$ degrees	Description
1	12.49993	0.025	86.603	−58.499	0.25-Hz comb
2	12.50002	−0.002	90.000	66.561	0.25-Hz comb
3	31.76207	−0.151	127.576	29.821	PowerFlux idx 66
4	36.60793	−0.416	161.240	−52.346	Present only in L1
5	36.60841	−0.075	100.874	43.930	Present only in L1
6	13.49980	0.055	93.007	58.722	0.25-Hz comb

(Table continued)

TABLE XIII. *(Continued)*

Idx	Frequency Hz	Spin-down nHz/s	RA_{J2000} degrees	DEC_{J2000} degrees	Description
7	31.76213	−0.029	121.201	−22.659	PowerFlux idx 66
8	85.82924	−0.782	122.451	42.487	Present only in H1
9	85.82951	0.014	91.251	−60.424	Present only in H1
10	83.44610	0.356	57.433	74.096	Instrumental artifact
11	83.44718	−0.188	100.706	−71.727	Instrumental artifact
12	26.30940	0.120	65.866	28.651	PowerFlux idx 104
13	31.37813	0.076	86.489	60.660	Hardware injection ip11
14	31.51095	−0.260	125.878	−30.969	Hardware injection ip11
15	13.49954	0.028	103.846	−33.555	0.25-Hz comb
16	34.82444	−0.178	125.214	−37.390	Present only in H1
17	34.82526	0.365	43.489	59.488	Present only in H1
18	26.34245	0.188	101.305	−41.914	PowerFlux idx 104
19	52.80802	0.272	75.131	46.185	Hardware injection ip5
20	52.80847	−0.217	86.346	−63.610	Hardware injection ip5
21	19.90049	−0.049	120.105	−66.933	Transient disturbance
22	108.85713	0.016	172.077	−30.650	Hardware injection ip3
23	108.85751	−0.190	156.197	11.273	Hardware injection ip3
24	191.02943	−8.248	19.785	8.689	Hardware injection ip8
25	191.02921	−8.461	10.399	−26.263	Hardware injection ip8
26	39.76317	−0.250	116.156	35.030	PowerFlux idx 77
27	39.76228	−0.111	120.585	−49.208	PowerFlux idx 77
28	210.38111	−0.719	111.146	−73.636	Present only in H1
29	146.16957	−7.664	74.426	19.212	Hardware injection ip6
30	146.16861	−6.847	9.592	−64.231	Hardware injection ip6
31	46.94798	0.037	120.395	66.304	PowerFlux idx 48
32	46.94859	0.059	107.507	−49.753	PowerFlux idx 48
33	93.89883	0.344	66.466	72.993	Present only in H1
34	93.89971	−0.084	94.143	−67.379	Present only in H1
35	33.33199	0.186	82.235	49.267	Present at the beginning in H1 and in the middle in L1
36	33.33191	0.147	101.592	−24.740	Present at the beginning in H1 and in the middle in L1
37	28.94735	−0.023	80.524	−62.043	Present only in H1
38	28.94644	0.217	56.600	61.593	Present only in H1
39	140.25111	−0.261	118.249	65.668	0.25-Hz comb
40	273.76680	0.022	279.363	−0.225	Present only in the first half of O1
41	66.75634	0.060	67.002	65.771	Present only in H1
42	286.11848	0.220	282.207	7.749	Present only in the first half of O1
43	27.94841	0.150	79.648	−46.995	Present only in H1
44	65.87802	−0.007	95.671	68.015	Present only in H1
45	65.87734	0.237	82.021	−39.834	Present only in H1
46	265.57578	−0.077	71.932	−57.608	Hardware injection ip0
47	364.34662	0.322	281.187	22.135	Present only in the first half of O1
48	43.74991	−0.110	87.628	−41.298	0.25-Hz comb
49	331.65142	0.296	301.174	−56.957	Present only in the first half of O1

[1] J. Aasi *et al.* (LIGO Scientific Collaboration), Advanced LIGO, Classical Quantum Gravity **32**, 115012 (2015).

[2] B. P. Abbott *et al.* (LIGO Scientific Collaboration), Setting upper limits on the strength of periodic gravitational waves from PSR J1939 + 213, Phys. Rev. D **69**, 082004 (2004).

[3] B. Abbott *et al.* (LIGO Scientific Collaboration), M. Kramer, and A. G. Lyne, Limits on Gravitational-Wave Emission from Selected Pulsars Using LIGO Data, Phys. Rev. Lett. **94**, 181103 (2005).

[4] B. Abbott *et al.* (LIGO Scientific Collaboration), M. Kramer, and A. G. Lyne, Upper limits on gravitational wave emission from 78 radio pulsars, Phys. Rev. D **76**, 042001 (2007).

[5] B. Abbott *et al.* (LIGO Scientific Collaboration), Beating the spin-down limit on gravitational wave emission from the Crab pulsar, Astrophys. J. Lett. **683**, L45 (2008).

[6] B. P. Abbott *et al.* (LIGO Scientific Collaboration and Virgo Collaboration), Searches for gravitational waves from known pulsars with S5 LIGO data, Astrophys. J. **713**, 671 (2010).

[7] J. Abadie *et al.* (LIGO Scientific Collaboration), First search for gravitational waves from the youngest known neutron star, Astrophys. J. **722**, 1504 (2010).

[8] J. Aasi *et al.* (LIGO Scientific Collaboration and Virgo Collaboration), Searches for continuous gravitational waves from nine young supernova remnants, Astrophys. J. **813**, 39 (2015).

[9] B. P. Abbott *et al.* (LIGO Scientific Collaboration and Virgo Collaboration), Search for continuous gravitational waves from neutron stars in globular cluster NGC 6544, Phys. Rev. D **95**, 082005 (2017).

[10] B. P. Abbott *et al.* (LIGO Scientific Collaboration), Searches for periodic gravitational waves from unknown isolated sources and Scorpius X-1: Results from the second LIGO science run, Phys. Rev. D **76**, 082001 (2007).

[11] B. P. Abbott *et al.* (LIGO Scientific Collaboration), First all-sky upper limits from LIGO on the strength of periodic gravitational waves using the Hough transform, Phys. Rev. D **72**, 102004 (2005).

[12] B. Abbott *et al.* (LIGO Scientific Collaboration), All-sky search for periodic gravitational waves in LIGO S4 data, Phys. Rev. D **77**, 022001 (2008).

[13] B. Abbott *et al.* (LIGO Scientific Collaboration), Einstein@Home search for periodic gravitational waves in LIGO S4 data, Phys. Rev. D **79**, 022001 (2009).

[14] B. P. Abbott *et al.* (LIGO Scientific Collaboration), All-sky LIGO Search for Periodic Gravitational Waves in the Early S5 Data, Phys. Rev. Lett. **102**, 111102 (2009).

[15] B. P. Abbott *et al.* (LIGO Scientific Collaboration), Einstein@Home search for periodic gravitational waves in early S5 LIGO data, Phys. Rev. D **80**, 042003 (2009).

[16] B. Abbott *et al.* (The LIGO and Virgo Scientific Collaboration), All-sky search for periodic gravitational waves in the full S5 data, Phys. Rev. D **85**, 022001 (2012).

[17] B. P. Abbott *et al.* (LIGO Scientific Collaboration), Einstein@Home all-sky search for periodic gravitational waves in LIGO S5 data, Phys. Rev. D **87**, 042001 (2013).

[18] J. Aasi *et al.* (LIGO Scientific Collaboration and Virgo Collaboration), Application of a Hough search for continuous gravitational waves on data from the 5th LIGO science run, Classical Quantum Gravity **31**, 085014 (2014).

[19] J. Aasi *et al.* (LIGO Scientific Collaboration and Virgo Collaboration), Implementation of an $\mathcal{F}$-statistic all-sky search for continuous gravitational waves in Virgo VSR1 data, Classical Quantum Gravity **31**, 165014 (2014).

[20] J. Aasi *et al.* (LIGO Scientific Collaboration and Virgo Collaboration), Comprehensive all-sky search for periodic gravitational waves in the sixth science run LIGO data, Phys. Rev. D **94**, 042002 (2016).

[21] B. P. Abbott *et al.* (LIGO Scientific Collaboration and Virgo Collaboration), Results of the deepest all-sky survey for continuous gravitational waves on LIGO S6 data, Phys. Rev. D **94**, 102002 (2016).

[22] J. Aasi *et al.* (LIGO Scientific Collaboration and Virgo Collaboration), Search of the Orion spur for continuous gravitational waves using a "loosely coherent" algorithm on data from LIGO interferometers, Phys. Rev. D **93**, 042006 (2016).

[23] Selvaganapathy J, P. K. Das, and P. Konar (The LIGO Scientific Collaboration and the Virgo Collaboration), First low-frequency all-sky search for continuous gravitational wave signals, Phys. Rev. D **93**, 116003 (2016).

[24] V. Dergachev, On blind searches for noise dominated signals: A loosely coherent approach, Classical Quantum Gravity **27**, 205017 (2010).

[25] V. Dergachev, Novel universal statistic for computing upper limits in ill-behaved background, Phys. Rev. D **87**, 062001 (2013).

[26] Sinead Walsh *et al.*, Comparison of methods for the detection of gravitational waves from unknown neutron stars, Phys. Rev. D **94**, 124010 (2016).

[27] P. Jaranowski, A. Królak, and B. F. Schutz, Data analysis of gravitational-wave signals from spinning neutron stars. I. The signal and its detection, Phys. Rev. D **58**, 063001 (1998).

[28] J. Aasi *et al.* (LIGO Scientific Collaboration and Virgo Collaboration), Characterization of the LIGO detectors during their sixth science run, Classical Quantum Gravity **32**, 115012 (2015).

[29] B. P. Abbott *et al.* (LIGO Scientific Collaboration and Virgo Collaboration), GW150914: The Advanced LIGO Detectors in the Era of First Discoveries, Phys. Rev. Lett. **116**, 131103 (2016).

[30] B. P. Abbott *et al.* (LIGO Scientific Collaboration and Virgo Collaboration), Upper Limits on the Stochastic Gravitational-Wave Background from Advanced LIGO's First Observing Run, Phys. Rev. Lett. **118**, 121101 (2017).

[31] M. A. Papa *et al.*, Hierarchical follow-up of subthreshold candidates of an all-sky Einstein@Home search for continuous gravitational waves on LIGO sixth science run data, Phys. Rev. D **94**, 122006 (2016).

[32] B. P. Abbott *et al.* (LIGO Scientific Collaboration and Virgo Collaboration), First low-frequency Einstein@Home all-sky search for continuous gravitational waves in Advanced LIGO data (to be published), http://dcc.ligo.org/LIGO-P1700127.

[33] V. Dergachev, LIGO Report No. LIGO-T050186, 2005.

[34] V. Dergachev, LIGO Report No. LIGO-T1000272, 2010.

[35] V. Dergachev and K. Riles, LIGO Report No. LIGO-T050187, 2005.
[36] V. Dergachev, Loosely coherent searches for sets of well-modeled signals, Phys. Rev. D **85**, 062003 (2012).
[37] F. Antonucci, P. Astone, S. D'Antonio, S. Frasca, and C. Palomba, Detection of periodic gravitational wave sources by Hough transform in the f versus $\dot{f}$ plane, Classical Quantum Gravity **25**, 184015 (2008).
[38] P. Astone, A. Colla, S. D'Antonio, S. Frasca, and C. Palomba, Method for all-sky searches of continuous gravitational wave signals using the FrequencyHough transform, Phys. Rev. D **90**, 042002 (2014).
[39] P. Astone, S. Frasca, and C. Palomba, The short FFT database and the peak map for the hierarchical search of periodic sources, Classical Quantum Gravity **22**, S1197 (2005).
[40] C. Palomba, P. Astone, and S. Frasca, Adaptive Hough transform for the search of periodic sources, Classical Quantum Gravity **22**, S1255 (2005).
[41] B. Krishnan, A. M. Sintes, M. A. Papa, B. F. Schutz, S. Frasca, and C. Palomba, Hough transform search for continuous gravitational waves, Phys. Rev. D **70**, 082001 (2004).
[42] A. M. Sintes and B. Krishnan, Improved Hough search for gravitational wave pulsars, J. Phys. Conf. Ser. **32**, 206 (2006).
[43] L. Sancho de la Jordana and A. M. Sintes, A χ^2 veto for continuous gravitational wave searches, Classical Quantum Gravity **25**, 184014 (2008).
[44] P. Covas, Master thesis, University of the Balearic Islands, LIGO Report No. LIGO-P1600302, 2016.
[45] P. Astone, K. M. Borkowski, P. Jaranowski, M. Pietka, and A. Królak, Data analysis of gravitational-wave signals from spinning neutron stars. V. A narrow-band all-sky search, Phys. Rev. D **82**, 022005 (2010).
[46] A. Pisarski and P. Jaranowski, Banks of templates for all-sky narrow-band searches of gravitational waves from spinning neutron stars, Classical Quantum Gravity **32**, 145014 (2015).
[47] See Supplemental Material http://link.aps.org/supplemental/10.1103/PhysRevD.96.062002 Document No. [number will be inserted by publisher] for numerical values of upper limits.
[48] C. Biwer *et al.*, Validating gravitational-wave detections: The Advanced LIGO hardware injection system, Phys. Rev. D **95**, 062002 (2017).
[49] P. Astone, A. Colla, A. D'Antonio, S. Frasca, C. Palomba, and R. Serafinelli, Method for narrow band search of continuous gravitational wave signals, Phys. Rev. D **89**, 062008 (2014).
[50] C. J. Horowitz and K. Kadau, Breaking Strain of Neutron Star Crust and Gravitational Waves, Phys. Rev. Lett. **102**, 191102 (2009).
[51] N. K. Johnson-McDaniel and B. J. Owen, Maximum elastic deformations of relativistic stars, Phys. Rev. D **88**, 044004 (2013).

B. P. Abbott,[1] R. Abbott,[1] T. D. Abbott,[2] F. Acernese,[3,4] K. Ackley,[5] C. Adams,[6] T. Adams,[7] P. Addesso,[8] R. X. Adhikari,[1] V. B. Adya,[9] C. Affeldt,[9] M. Afrough,[10] B. Agarwal,[11] K. Agatsuma,[12] N. Aggarwal,[13] O. D. Aguiar,[14] L. Aiello,[15,16] A. Ain,[17] P. Ajith,[18] B. Allen,[9,19,20] G. Allen,[11] A. Allocca,[21,22] P. A. Altin,[23] A. Amato,[24] A. Ananyeva,[1] S. B. Anderson,[1] W. G. Anderson,[19] S. Antier,[25] S. Appert,[1] K. Arai,[1] M. C. Araya,[1] J. S. Areeda,[26] N. Arnaud,[25,27] S. Ascenzi,[28,16] G. Ashton,[9] M. Ast,[29] S. M. Aston,[6] P. Astone,[30] P. Aufmuth,[20] C. Aulbert,[9] K. AultONeal,[31] A. Avila-Alvarez,[26] S. Babak,[32] P. Bacon,[33] M. K. M. Bader,[12] S. Bae,[34] P. T. Baker,[35,36] F. Baldaccini,[37,38] G. Ballardin,[27] S. W. Ballmer,[39] S. Banagiri,[40] J. C. Barayoga,[1] S. E. Barclay,[41] B. C. Barish,[1] D. Barker,[42] F. Barone,[3,4] B. Barr,[41] L. Barsotti,[13] M. Barsuglia,[33] D. Barta,[43] J. Bartlett,[42] I. Bartos,[44] R. Bassiri,[45] A. Basti,[21,22] J. C. Batch,[42] C. Baune,[9] M. Bawaj,[46,38] M. Bazzan,[47,48] B. Bécsy,[49] C. Beer,[9] M. Bejger,[50] I. Belahcene,[25] A. S. Bell,[41] B. K. Berger,[1] G. Bergmann,[9] C. P. L. Berry,[51] D. Bersanetti,[52,53] A. Bertolini,[12] J. Betzwieser,[6] S. Bhagwat,[39] R. Bhandare,[54] I. A. Bilenko,[55] G. Billingsley,[1] C. R. Billman,[5] J. Birch,[6] R. Birney,[56] O. Birnholtz,[9] S. Biscans,[13] A. Bisht,[20] M. Bitossi,[27,22] C. Biwer,[39] M. A. Bizouard,[25] J. K. Blackburn,[1] J. Blackman,[57] C. D. Blair,[58] D. G. Blair,[58] R. M. Blair,[42] S. Bloemen,[59] O. Bock,[9] N. Bode,[9] M. Boer,[60] G. Bogaert,[60] A. Bohe,[32] F. Bondu,[61] R. Bonnand,[7] B. A. Boom,[12] R. Bork,[1] V. Boschi,[21,22] S. Bose,[62,17] Y. Bouffanais,[33] A. Bozzi,[27] C. Bradaschia,[22] P. R. Brady,[19] V. B. Braginsky,[55,†] M. Branchesi,[63,64] J. E. Brau,[65] T. Briant,[66] A. Brillet,[60] M. Brinkmann,[9] V. Brisson,[25] P. Brockill,[19] J. E. Broida,[67] A. F. Brooks,[1] D. A. Brown,[39] D. D. Brown,[51] N. M. Brown,[13] S. Brunett,[1] C. C. Buchanan,[2] A. Buikema,[13] T. Bulik,[68] H. J. Bulten,[69,12] A. Buonanno,[32,70] D. Buskulic,[7] C. Buy,[33] R. L. Byer,[45] M. Cabero,[9] L. Cadonati,[71] G. Cagnoli,[24,72] C. Cahillane,[1] J. Calderón Bustillo,[71] T. A. Callister,[1] E. Calloni,[73,4] J. B. Camp,[74] P. Canizares,[59] K. C. Cannon,[75] H. Cao,[76] J. Cao,[77] C. D. Capano,[9] E. Capocasa,[33] F. Carbognani,[27] S. Caride,[78] M. F. Carney,[79] J. Casanueva Diaz,[25] C. Casentini,[28,16] S. Caudill,[19] M. Cavaglià,[10] F. Cavalier,[25] R. Cavalieri,[27] G. Cella,[22] C. B. Cepeda,[1] L. Cerboni Baiardi,[63,64] G. Cerretani,[21,22] E. Cesarini,[28,16] S. J. Chamberlin,[80] M. Chan,[41] S. Chao,[81] P. Charlton,[82] E. Chassande-Mottin,[33] D. Chatterjee,[19] B. D. Cheeseboro,[35,36] H. Y. Chen,[84] Y. Chen,[57] H.-P. Cheng,[5] A. Chincarini,[53] A. Chiummo,[27] T. Chmiel,[79] H. S. Cho,[85] M. Cho,[70] J. H. Chow,[23] N. Christensen,[67,60] Q. Chu,[58] A. J. K. Chua,[86] S. Chua,[66] A. K. W. Chung,[87] S. Chung,[58] G. Ciani,[5] P. Ciecielag,[50] R. Ciolfi,[88,89] C. E. Cirelli,[45] A. Cirone,[52,53] F. Clara,[42] J. A. Clark,[71] F. Cleva,[60] C. Cocchieri,[10] E. Coccia,[15,16]

P.-F. Cohadon,[66] A. Colla,[90,30] C. G. Collette,[91] L. R. Cominsky,[92] M. Constancio Jr.,[14] L. Conti,[48] S. J. Cooper,[51] P. Corban,[6] T. R. Corbitt,[2] K. R. Corley,[44] N. Cornish,[93] A. Corsi,[78] S. Cortese,[27] C. A. Costa,[14] E. Coughlin,[67] M. W. Coughlin,[67] S. B. Coughlin,[94,95] J.-P. Coulon,[60] S. T. Countryman,[44] P. Couvares,[1] P. B. Covas,[96] E. E. Cowan,[71] D. M. Coward,[58] M. J. Cowart,[6] D. C. Coyne,[1] R. Coyne,[78] J. D. E. Creighton,[19] T. D. Creighton,[97] J. Cripe,[2] S. G. Crowder,[98] T. J. Cullen,[26] A. Cumming,[41] L. Cunningham,[41] E. Cuoco,[27] T. Dal Canton,[74] S. L. Danilishin,[20,9] S. D'Antonio,[16] K. Danzmann,[20,9] A. Dasgupta,[99] C. F. Da Silva Costa,[5] V. Dattilo,[27] I. Dave,[54] M. Davier,[25] D. Davis,[39] E. J. Daw,[100] B. Day,[71] S. De,[39] D. DeBra,[45] E. Deelman,[101] J. Degallaix,[24] M. De Laurentis,[73,4] S. Deléglise,[66] W. Del Pozzo,[51,21,22] T. Denker,[9] T. Dent,[9] V. Dergachev,[32] R. De Rosa,[73,4] R. T. DeRosa,[6] R. DeSalvo,[102] J. Devenson,[56] R. C. Devine,[35,36] S. Dhurandhar,[17] M. C. Díaz,[97] L. Di Fiore,[4] M. Di Giovanni,[103,89] T. Di Girolamo,[73,4,44] A. Di Lieto,[21,22] S. Di Pace,[90,30] I. Di Palma,[90,30] F. Di Renzo,[21,22] Z. Doctor,[84] V. Dolique,[24] F. Donovan,[13] K. L. Dooley,[10] S. Doravari,[9] O. Dorosh,[124] I. Dorrington,[95] R. Douglas,[41] M. Dovale Álvarez,[51] T. P. Downes,[19] M. Drago,[9] R. W. P. Drever,[1,†] J. C. Driggers,[42] Z. Du,[77] M. Ducrot,[7] J. Duncan,[94] S. E. Dwyer,[42] T. B. Edo,[100] M. C. Edwards,[67] A. Effler,[6] H.-B. Eggenstein,[9] P. Ehrens,[1] J. Eichholz,[1] S. S. Eikenberry,[5] R. A. Eisenstein,[13] R. C. Essick,[13] Z. B. Etienne,[35,36] T. Etzel,[1] M. Evans,[13] T. M. Evans,[6] M. Factourovich,[44] V. Fafone,[28,16,15] H. Fair,[39] S. Fairhurst,[95] X. Fan,[77] S. Farinon,[53] B. Farr,[84] W. M. Farr,[51] E. J. Fauchon-Jones,[95] M. Favata,[104] M. Fays,[95] H. Fehrmann,[9] J. Feicht,[1] M. M. Fejer,[45] A. Fernandez-Galiana,[13] I. Ferrante,[21,22] E. C. Ferreira,[14] F. Ferrini,[27] F. Fidecaro,[21,22] I. Fiori,[27] D. Fiorucci,[33] R. P. Fisher,[39] R. Flaminio,[24,105] M. Fletcher,[41] H. Fong,[83] P. W. F. Forsyth,[23] S. S. Forsyth,[71] J.-D. Fournier,[60] S. Frasca,[90,30] F. Frasconi,[22] Z. Frei,[49] A. Freise,[51] R. Frey,[65] V. Frey,[25] E. M. Fries,[1] P. Fritschel,[13] V. V. Frolov,[6] P. Fulda,[5,74] M. Fyffe,[6] H. Gabbard,[9] M. Gabel,[106] B. U. Gadre,[17] S. M. Gaebel,[51] J. R. Gair,[107] L. Gammaitoni,[37] M. R. Ganija,[76] S. G. Gaonkar,[17] F. Garufi,[73,4] S. Gaudio,[31] G. Gaur,[108] V. Gayathri,[109] N. Gehrels,[74,†] G. Gemme,[53] E. Genin,[27] A. Gennai,[22] D. George,[11] J. George,[54] L. Gergely,[110] V. Germain,[7] S. Ghonge,[71] Abhirup Ghosh,[18] Archisman Ghosh,[18,12] S. Ghosh,[59,12] J. A. Giaime,[2,6] K. D. Giardina,[6] A. Giazotto,[22] K. Gill,[31] L. Glover,[102] E. Goetz,[9] R. Goetz,[5] S. Gomes,[95] G. González,[2] J. M. Gonzalez Castro,[21,22] A. Gopakumar,[111] M. L. Gorodetsky,[55] S. E. Gossan,[1] M. Gosselin,[27] R. Gouaty,[7] A. Grado,[112,4] C. Graef,[41] M. Granata,[24] A. Grant,[41] S. Gras,[13] C. Gray,[42] G. Greco,[63,64] A. C. Green,[51] P. Groot,[59] H. Grote,[9] S. Grunewald,[32] P. Gruning,[25] G. M. Guidi,[63,64] X. Guo,[77] A. Gupta,[80] M. K. Gupta,[99] K. E. Gushwa,[1] E. K. Gustafson,[1] R. Gustafson,[113] B. R. Hall,[62] E. D. Hall,[1] G. Hammond,[41] M. Haney,[111] M. M. Hanke,[9] J. Hanks,[42] C. Hanna,[80] O. A. Hannuksela,[87] J. Hanson,[6] T. Hardwick,[2] J. Harms,[63,64] G. M. Harry,[114] I. W. Harry,[32] M. J. Hart,[41] C.-J. Haster,[83] K. Haughian,[41] J. Healy,[115] A. Heidmann,[66] M. C. Heintze,[6] H. Heitmann,[60] P. Hello,[25] G. Hemming,[27] M. Hendry,[41] I. S. Heng,[41] J. Hennig,[41] J. Henry,[115] A. W. Heptonstall,[1] M. Heurs,[9,20] S. Hild,[41] D. Hoak,[27] D. Hofman,[24] K. Holt,[6] D. E. Holz,[84] P. Hopkins,[95] C. Horst,[19] J. Hough,[41] E. A. Houston,[41] E. J. Howell,[58] Y. M. Hu,[9] E. A. Huerta,[11] D. Huet,[25] B. Hughey,[31] S. Husa,[96] S. H. Huttner,[41] T. Huynh-Dinh,[6] N. Indik,[9] D. R. Ingram,[42] R. Inta,[78] G. Intini,[90,30] H. N. Isa,[41] J.-M. Isac,[66] M. Isi,[1] B. R. Iyer,[18] K. Izumi,[42] T. Jacqmin,[66] K. Jani,[71] P. Jaranowski,[116] S. Jawahar,[117] F. Jiménez-Forteza,[96] W. W. Johnson,[2] D. I. Jones,[118] R. Jones,[41] R. J. G. Jonker,[12] L. Ju,[58] J. Junker,[9] C. V. Kalaghatgi,[95] V. Kalogera,[94] S. Kandhasamy,[6] G. Kang,[34] J. B. Kanner,[1] S. Karki,[65] K. S. Karvinen,[9] M. Kasprzack,[2] M. Katolik,[11] E. Katsavounidis,[13] W. Katzman,[6] S. Kaufer,[20] K. Kawabe,[42] F. Kéfélian,[60] D. Keitel,[41] A. J. Kemball,[11] R. Kennedy,[100] C. Kent,[95] J. S. Key,[119] F. Y. Khalili,[55] I. Khan,[15,16] S. Khan,[9] Z. Khan,[99] E. A. Khazanov,[120] N. Kijbunchoo,[42] Chunglee Kim,[121] J. C. Kim,[122] W. Kim,[76] W. S. Kim,[123] Y.-M. Kim,[85,121] S. J. Kimbrell,[71] E. J. King,[76] P. J. King,[42] R. Kirchhoff,[9] J. S. Kissel,[42] L. Kleybolte,[29] S. Klimenko,[5] P. Koch,[9] S. M. Koehlenbeck,[9] S. Koley,[12] V. Kondrashov,[1] A. Kontos,[13] M. Korobko,[29] W. Z. Korth,[1] I. Kowalska,[68] D. B. Kozak,[1] C. Krämer,[9] V. Kringel,[9] B. Krishnan,[9] A. Królak,[124,125] G. Kuehn,[9] P. Kumar,[83] R. Kumar,[99] S. Kumar,[18] L. Kuo,[81] A. Kutynia,[124] S. Kwang,[19] B. D. Lackey,[32] K. H. Lai,[87] M. Landry,[42] R. N. Lang,[19] J. Lange,[115] B. Lantz,[45] R. K. Lanza,[13] A. Lartaux-Vollard,[25] P. D. Lasky,[126] M. Laxen,[6] A. Lazzarini,[1] C. Lazzaro,[48] P. Leaci,[90,30] S. Leavey,[41] C. H. Lee,[85] H. K. Lee,[127] H. M. Lee,[121] H. W. Lee,[122] K. Lee,[41] J. Lehmann,[9] A. Lenon,[35,36] M. Leonardi,[103,89] N. Leroy,[25] N. Letendre,[7] Y. Levin,[126] T. G. F. Li,[87] A. Libson,[13] T. B. Littenberg,[128] J. Liu,[58] W. Liu,[113] R. K. L. Lo,[87] N. A. Lockerbie,[117] L. T. London,[95] J. E. Lord,[39] M. Lorenzini,[15,16] V. Loriette,[129] M. Lormand,[6] G. Losurdo,[22] J. D. Lough,[9,20] G. Lovelace,[26] H. Lück,[20,9] D. Lumaca,[28,16] A. P. Lundgren,[9] R. Lynch,[13] Y. Ma,[57] S. Macfoy,[56] B. Machenschalk,[9] M. MacInnis,[13] D. M. Macleod,[2] I. Magaña Hernandez,[87] F. Magaña-Sandoval,[39] L. Magaña Zertuche,[39] R. M. Magee,[80] E. Majorana,[30] I. Maksimovic,[129] N. Man,[60] V. Mandic,[40] V. Mangano,[41] G. L. Mansell,[23] M. Manske,[19] M. Mantovani,[27] F. Marchesoni,[46,38] F. Marion,[7] S. Márka,[44] Z. Márka,[44] C. Markakis,[11] A. S. Markosyan,[45] E. Maros,[1] F. Martelli,[63,64] L. Martellini,[60] I. W. Martin,[41] D. V. Martynov,[13] J. N. Marx,[1] K. Mason,[13]

A. Masserot,[7] T. J. Massinger,[1] M. Masso-Reid,[41] S. Mastrogiovanni,[90,30] A. Matas,[40] F. Matichard,[13] L. Matone,[44] N. Mavalvala,[13] R. Mayani,[101] N. Mazumder,[62] R. McCarthy,[42] D. E. McClelland,[23] S. McCormick,[6] L. McCuller,[13] S. C. McGuire,[130] G. McIntyre,[1] J. McIver,[1] D. J. McManus,[23] T. McRae,[23] S. T. McWilliams,[35,36] D. Meacher,[80] G. D. Meadors,[32,9] J. Meidam,[12] E. Mejuto-Villa,[8] A. Melatos,[131] G. Mendell,[42] R. A. Mercer,[19] E. L. Merilh,[42] M. Merzougui,[60] S. Meshkov,[1] C. Messenger,[41] C. Messick,[80] R. Metzdorff,[66] P. M. Meyers,[40] F. Mezzani,[30,90] H. Miao,[51] C. Michel,[24] H. Middleton,[51] E. E. Mikhailov,[132] L. Milano,[73,4] A. L. Miller,[5] A. Miller,[90,30] B. B. Miller,[94] J. Miller,[13] M. Millhouse,[93] O. Minazzoli,[60] Y. Minenkov,[16] J. Ming,[32] C. Mishra,[133] S. Mitra,[17] V. P. Mitrofanov,[55] G. Mitselmakher,[5] R. Mittleman,[13] A. Moggi,[22] M. Mohan,[27] S. R. P. Mohapatra,[13] M. Montani,[63,64] B. C. Moore,[104] C. J. Moore,[86] D. Moraru,[42] G. Moreno,[42] S. R. Morriss,[97] B. Mours,[7] C. M. Mow-Lowry,[51] G. Mueller,[5] A. W. Muir,[95] Arunava Mukherjee,[9] D. Mukherjee,[19] S. Mukherjee,[97] N. Mukund,[17] A. Mullavey,[6] J. Munch,[76] E. A. M. Muniz,[39] P. G. Murray,[41] K. Napier,[71] I. Nardecchia,[28,16] L. Naticchioni,[90,30] R. K. Nayak,[134] G. Nelemans,[59,12] T. J. N. Nelson,[6] M. Neri,[52,53] M. Nery,[9] A. Neunzert,[113] J. M. Newport,[114] G. Newton,[41,†] K. K. Y. Ng,[87] T. T. Nguyen,[23] D. Nichols,[59] A. B. Nielsen,[9] S. Nissanke,[59,12] A. Nitz,[9] A. Noack,[9] F. Nocera,[27] D. Nolting,[6] M. E. N. Normandin,[97] L. K. Nuttall,[39] J. Oberling,[42] E. Ochsner,[19] E. Oelker,[13] G. H. Ogin,[106] J. J. Oh,[123] S. H. Oh,[123] F. Ohme,[9] M. Oliver,[96] P. Oppermann,[9] Richard J. Oram,[6] B. O'Reilly,[6] R. Ormiston,[40] L. F. Ortega,[5] R. O'Shaughnessy,[115] D. J. Ottaway,[76] H. Overmier,[6] B. J. Owen,[78] A. E. Pace,[80] J. Page,[128] M. A. Page,[58] A. Pai,[109] S. A. Pai,[54] J. R. Palamos,[65] O. Palashov,[120] C. Palomba,[30] A. Pal-Singh,[29] H. Pan,[81] B. Pang,[57] P. T. H. Pang,[87] C. Pankow,[94] F. Pannarale,[95] B. C. Pant,[54] F. Paoletti,[22] A. Paoli,[27] M. A. Papa,[32,19,9] H. R. Paris,[45] W. Parker,[6] D. Pascucci,[41] A. Pasqualetti,[27] R. Passaquieti,[21,22] D. Passuello,[22] B. Patricelli,[135,22] B. L. Pearlstone,[41] M. Pedraza,[1] R. Pedurand,[24,136] L. Pekowsky,[39] A. Pele,[6] S. Penn,[137] C. J. Perez,[42] A. Perreca,[1,103,89] L. M. Perri,[94] H. P. Pfeiffer,[83] M. Phelps,[41] O. J. Piccinni,[90,30] M. Pichot,[60] F. Piergiovanni,[63,64] V. Pierro,[8] G. Pillant,[27] L. Pinard,[24] I. M. Pinto,[8] A. Pisarski,[116] M. Pitkin,[41] R. Poggiani,[21,22] P. Popolizio,[27] E. K. Porter,[33] A. Post,[9] J. Powell,[41] J. Prasad,[17] J. W. W. Pratt,[31] V. Predoi,[95] T. Prestegard,[19] M. Prijatelj,[9] M. Principe,[8] S. Privitera,[32] R. Prix,[9] G. A. Prodi,[103,89] L. G. Prokhorov,[55] O. Puncken,[9] M. Punturo,[38] P. Puppo,[30] M. Pürrer,[32] H. Qi,[19] J. Qin,[58] S. Qiu,[126] V. Quetschke,[97] E. A. Quintero,[1] R. Quitzow-James,[65] F. J. Raab,[42] D. S. Rabeling,[23] H. Radkins,[42] P. Raffai,[49] S. Raja,[54] C. Rajan,[54] M. Rakhmanov,[97] K. E. Ramirez,[97] P. Rapagnani,[90,30] V. Raymond,[32] M. Razzano,[21,22] J. Read,[26] T. Regimbau,[60] L. Rei,[53] S. Reid,[56] D. H. Reitze,[1,5] H. Rew,[132] S. D. Reyes,[39] F. Ricci,[90,30] P. M. Ricker,[11] S. Rieger,[9] K. Riles,[113] M. Rizzo,[115] N. A. Robertson,[1,41] R. Robie,[41] F. Robinet,[25] A. Rocchi,[16] L. Rolland,[7] J. G. Rollins,[1] V. J. Roma,[65] R. Romano,[3,4] C. L. Romel,[42] J. H. Romie,[6] D. Rosińska,[138,50] M. P. Ross,[139] S. Rowan,[41] A. Rüdiger,[9] P. Ruggi,[27] K. Ryan,[42] M. Rynge,[101] S. Sachdev,[1] T. Sadecki,[42] L. Sadeghian,[19] M. Sakellariadou,[140] L. Salconi,[27] M. Saleem,[109] F. Salemi,[9] A. Samajdar,[134] L. Sammut,[126] L. M. Sampson,[94] E. J. Sanchez,[1] V. Sandberg,[42] B. Sandeen,[94] J. R. Sanders,[39] B. Sassolas,[24] P. R. Saulson,[39] O. Sauter,[113] R. L. Savage,[42] A. Sawadsky,[20] P. Schale,[65] J. Scheuer,[94] E. Schmidt,[31] J. Schmidt,[9] P. Schmidt,[1,59] R. Schnabel,[29] R. M. S. Schofield,[65] A. Schönbeck,[29] E. Schreiber,[9] D. Schuette,[9,20] B. W. Schulte,[9] B. F. Schutz,[95,9] S. G. Schwalbe,[31] J. Scott,[41] S. M. Scott,[23] E. Seidel,[11] D. Sellers,[6] A. S. Sengupta,[141] D. Sentenac,[27] V. Sequino,[28,16] A. Sergeev,[120] D. A. Shaddock,[23] T. J. Shaffer,[42] A. A. Shah,[128] M. S. Shahriar,[94] L. Shao,[32] B. Shapiro,[45] P. Shawhan,[70] A. Sheperd,[19] D. H. Shoemaker,[13] D. M. Shoemaker,[71] K. Siellez,[71] X. Siemens,[19] M. Sieniawska,[50] D. Sigg,[42] A. D. Silva,[14] A. Singer,[1] L. P. Singer,[74] A. Singh,[32,9,20] R. Singh,[2] A. Singhal,[15,30] A. M. Sintes,[96] B. J. J. Slagmolen,[23] B. Smith,[6] J. R. Smith,[26] R. J. E. Smith,[1] E. J. Son,[123] J. A. Sonnenberg,[19] B. Sorazu,[41] F. Sorrentino,[53] T. Souradeep,[17] A. P. Spencer,[41] A. K. Srivastava,[99] A. Staley,[44] M. Steinke,[9] J. Steinlechner,[41,29] S. Steinlechner,[29] D. Steinmeyer,[9,20] B. C. Stephens,[19] R. Stone,[97] K. A. Strain,[41] G. Stratta,[63,64] S. E. Strigin,[55] R. Sturani,[142] A. L. Stuver,[6] T. Z. Summerscales,[143] L. Sun,[131] S. Sunil,[99] P. J. Sutton,[95] B. L. Swinkels,[27] M. J. Szczepańczyk,[31] M. Tacca,[33] D. Talukder,[65] D. B. Tanner,[5] D. Tao,[67] M. Tápai,[110] A. Taracchini,[32] J. A. Taylor,[128] R. Taylor,[1] T. Theeg,[9] E. G. Thomas,[51] M. Thomas,[6] P. Thomas,[42] K. A. Thorne,[6] K. S. Thorne,[57] E. Thrane,[126] S. Tiwari,[15,89] V. Tiwari,[95] K. V. Tokmakov,[117] K. Toland,[41] M. Tonelli,[21,22] Z. Tornasi,[41] C. I. Torrie,[1] D. Töyrä,[51] F. Travasso,[27,38] G. Traylor,[6] S. Trembath-Reichert,[113] D. Trifirò,[10] J. Trinastic,[5] M. C. Tringali,[103,89] L. Trozzo,[144,22] K. W. Tsang,[12] M. Tse,[13] R. Tso,[1] D. Tuyenbayev,[97] K. Ueno,[19] D. Ugolini,[145] C. S. Unnikrishnan,[111] A. L. Urban,[1] S. A. Usman,[95] K. Vahi,[101] H. Vahlbruch,[20] G. Vajente,[1] G. Valdes,[97] M. Vallisneri,[57] N. van Bakel,[12] M. van Beuzekom,[12] J. F. J. van den Brand,[69,12] C. Van Den Broeck,[12] D. C. Vander-Hyde,[39] L. van der Schaaf,[12] J. V. van Heijningen,[12] A. A. van Veggel,[41] M. Vardaro,[47,48] V. Varma,[57] S. Vass,[1] M. Vasúth,[43] A. Vecchio,[51] G. Vedovato,[48] J. Veitch,[51] P. J. Veitch,[76] K. Venkateswara,[139] G. Venugopalan,[1] D. Verkindt,[7] F. Vetrano,[63,64] A. Viceré,[63,64] A. D. Viets,[19] S. Vinciguerra,[51] D. J. Vine,[56] J.-Y. Vinet,[60]

S. Vitale,[13] T. Vo,[39] H. Vocca,[37,38] C. Vorvick,[42] D. V. Voss,[5] W. D. Vousden,[51] S. P. Vyatchanin,[55] A. R. Wade,[1] L. E. Wade,[79] M. Wade,[79] R. Walet,[12] M. Walker,[2] L. Wallace,[1] S. Walsh,[19] G. Wang,[15,64] H. Wang,[51] J. Z. Wang,[80] M. Wang,[51] Y.-F. Wang,[87] Y. Wang,[58] R. L. Ward,[23] J. Warner,[42] M. Was,[7] J. Watchi,[91] B. Weaver,[42] L.-W. Wei,[9,20] M. Weinert,[9] A. J. Weinstein,[1] R. Weiss,[13] L. Wen,[58] E. K. Wessel,[11] P. Weßels,[9] T. Westphal,[9] K. Wette,[9] J. T. Whelan,[115] B. F. Whiting,[5] C. Whittle,[126] D. Williams,[41] R. D. Williams,[1] A. R. Williamson,[115] J. L. Willis,[146] B. Willke,[20,9] M. H. Wimmer,[9,20] W. Winkler,[9] C. C. Wipf,[1] H. Wittel,[9,20] G. Woan,[41] J. Woehler,[9] J. Wofford,[115] K. W. K. Wong,[87] J. Worden,[42] J. L. Wright,[41] D. S. Wu,[9] G. Wu,[6] W. Yam,[13] H. Yamamoto,[1] C. C. Yancey,[70] M. J. Yap,[23] Hang Yu,[13] Haocun Yu,[13] M. Yvert,[7] A. Zadrożny,[124] M. Zanolin,[31] T. Zelenova,[27] J.-P. Zendri,[48] M. Zevin,[94] L. Zhang,[1] M. Zhang,[132] T. Zhang,[41] Y.-H. Zhang,[115] C. Zhao,[58] M. Zhou,[94] Z. Zhou,[94] S. Zhu,[32] X. J. Zhu,[58] M. E. Zucker,[1,13] and J. Zweizig[1]

(LIGO Scientific Collaboration and Virgo Collaboration)

[1]*LIGO, California Institute of Technology, Pasadena, California 91125, USA*
[2]*Louisiana State University, Baton Rouge, Louisiana 70803, USA*
[3]*Università di Salerno, Fisciano, I-84084 Salerno, Italy*
[4]*INFN, Sezione di Napoli, Complesso Universitario di Monte S.Angelo, I-80126 Napoli, Italy*
[5]*University of Florida, Gainesville, Florida 32611, USA*
[6]*LIGO Livingston Observatory, Livingston, Louisiana 70754, USA*
[7]*Laboratoire d'Annecy-le-Vieux de Physique des Particules (LAPP), Université Savoie Mont Blanc, CNRS/IN2P3, F-74941 Annecy, France*
[8]*University of Sannio at Benevento, I-82100 Benevento, Italy and INFN, Sezione di Napoli, I-80100 Napoli, Italy*
[9]*Albert-Einstein-Institut, Max-Planck-Institut für Gravitationsphysik, D-30167 Hannover, Germany*
[10]*The University of Mississippi, University, Mississippi 38677, USA*
[11]*NCSA, University of Illinois at Urbana-Champaign, Urbana, Illinois 61801, USA*
[12]*Nikhef, Science Park, 1098 XG Amsterdam, The Netherlands*
[13]*LIGO, Massachusetts Institute of Technology, Cambridge, Massachusetts 02139, USA*
[14]*Instituto Nacional de Pesquisas Espaciais, 12227-010 São José dos Campos, São Paulo, Brazil*
[15]*Gran Sasso Science Institute (GSSI), I-67100 L'Aquila, Italy*
[16]*INFN, Sezione di Roma Tor Vergata, I-00133 Roma, Italy*
[17]*Inter-University Centre for Astronomy and Astrophysics, Pune 411007, India*
[18]*International Centre for Theoretical Sciences, Tata Institute of Fundamental Research, Bengaluru 560089, India*
[19]*University of Wisconsin-Milwaukee, Milwaukee, Wisconsin 53201, USA*
[20]*Leibniz Universität Hannover, D-30167 Hannover, Germany*
[21]*Università di Pisa, I-56127 Pisa, Italy*
[22]*INFN, Sezione di Pisa, I-56127 Pisa, Italy*
[23]*OzGrav, Australian National University, Canberra, Australian Capital Territory 0200, Australia*
[24]*Laboratoire des Matériaux Avancés (LMA), CNRS/IN2P3, F-69622 Villeurbanne, France*
[25]*LAL, Univ. Paris-Sud, CNRS/IN2P3, Université Paris-Saclay, F-91898 Orsay, France*
[26]*California State University Fullerton, Fullerton, California 92831, USA*
[27]*European Gravitational Observatory (EGO), I-56021 Cascina, Pisa, Italy*
[28]*Università di Roma Tor Vergata, I-00133 Roma, Italy*
[29]*Universität Hamburg, D-22761 Hamburg, Germany*
[30]*INFN, Sezione di Roma, I-00185 Roma, Italy*
[31]*Embry-Riddle Aeronautical University, Prescott, Arizona 86301, USA*
[32]*Albert-Einstein-Institut, Max-Planck-Institut für Gravitationsphysik, D-14476 Potsdam-Golm, Germany*
[33]*APC, AstroParticule et Cosmologie, Université Paris Diderot, CNRS/IN2P3, CEA/Irfu, Observatoire de Paris, Sorbonne Paris Cité, F-75205 Paris Cedex 13, France*
[34]*Korea Institute of Science and Technology Information, Daejeon 34141, Korea*
[35]*West Virginia University, Morgantown, West Virginia 26506, USA*
[36]*Center for Gravitational Waves and Cosmology, West Virginia University, Morgantown, West Virginia 26505, USA*

[37]Università di Perugia, I-06123 Perugia, Italy
[38]INFN, Sezione di Perugia, I-06123 Perugia, Italy
[39]Syracuse University, Syracuse, New York 13244, USA
[40]University of Minnesota, Minneapolis, Minnesota 55455, USA
[41]SUPA, University of Glasgow, Glasgow G12 8QQ, United Kingdom
[42]LIGO Hanford Observatory, Richland, Washington 99352, USA
[43]Wigner RCP, RMKI, H-1121 Budapest, Konkoly Thege Miklós út 29-33, Hungary
[44]Columbia University, New York, New York 10027, USA
[45]Stanford University, Stanford, California 94305, USA
[46]Università di Camerino, Dipartimento di Fisica, I-62032 Camerino, Italy
[47]Università di Padova, Dipartimento di Fisica e Astronomia, I-35131 Padova, Italy
[48]INFN, Sezione di Padova, I-35131 Padova, Italy
[49]MTA Eötvös University, "Lendulet" Astrophysics Research Group, Budapest 1117, Hungary
[50]Nicolaus Copernicus Astronomical Center, Polish Academy of Sciences, 00-716 Warsaw, Poland
[51]University of Birmingham, Birmingham B15 2TT, United Kingdom
[52]Università degli Studi di Genova, I-16146 Genova, Italy
[53]INFN, Sezione di Genova, I-16146 Genova, Italy
[54]RRCAT, Indore Madhya Pradesh 452013, India
[55]Faculty of Physics, Lomonosov Moscow State University, Moscow 119991, Russia
[56]SUPA, University of the West of Scotland, Paisley PA1 2BE, United Kingdom
[57]Caltech CaRT, Pasadena, California 91125, USA
[58]OzGrav, University of Western Australia, Crawley, Western Australia 6009, Australia
[59]Department of Astrophysics/IMAPP, Radboud University Nijmegen,
P.O. Box 9010, 6500 GL Nijmegen, The Netherlands
[60]Artemis, Université Côte d'Azur, Observatoire Côte d'Azur, CNRS,
CS 34229, F-06304 Nice Cedex 4, France
[61]Institut de Physique de Rennes, CNRS, Université de Rennes 1, F-35042 Rennes, France
[62]Washington State University, Pullman, Washington 99164, USA
[63]Università degli Studi di Urbino 'Carlo Bo', I-61029 Urbino, Italy
[64]INFN, Sezione di Firenze, I-50019 Sesto Fiorentino, Firenze, Italy
[65]University of Oregon, Eugene, Oregon 97403, USA
[66]Laboratoire Kastler Brossel, UPMC-Sorbonne Universités, CNRS, ENS-PSL Research University,
Collège de France, F-75005 Paris, France
[67]Carleton College, Northfield, Minnesota 55057, USA
[68]Astronomical Observatory Warsaw University, 00-478 Warsaw, Poland
[69]VU University Amsterdam, 1081 HV Amsterdam, The Netherlands
[70]University of Maryland, College Park, Maryland 20742, USA
[71]Center for Relativistic Astrophysics and School of Physics, Georgia Institute of Technology,
Atlanta, Georgia 30332, USA
[72]Université Claude Bernard Lyon 1, F-69622 Villeurbanne, France
[73]Università di Napoli 'Federico II', Complesso Universitario di Monte S.Angelo, I-80126 Napoli, Italy
[74]NASA Goddard Space Flight Center, Greenbelt, Maryland 20771, USA
[75]RESCEU, University of Tokyo, Tokyo 113-0033, Japan
[76]OzGrav, University of Adelaide, Adelaide, South Australia 5005, Australia
[77]Tsinghua University, Beijing 100084, China
[78]Texas Tech University, Lubbock, Texas 79409, USA
[79]Kenyon College, Gambier, Ohio 43022, USA
[80]The Pennsylvania State University, University Park, Pennsylvania 16802, USA
[81]National Tsing Hua University, Hsinchu City, 30013 Taiwan, Republic of China
[82]Charles Sturt University, Wagga Wagga, New South Wales 2678, Australia
[83]Canadian Institute for Theoretical Astrophysics, University of Toronto,
Toronto, Ontario M5S 3H8, Canada
[84]University of Chicago, Chicago, Illinois 60637, USA
[85]Pusan National University, Busan 46241, Korea
[86]University of Cambridge, Cambridge CB2 1TN, United Kingdom
[87]The Chinese University of Hong Kong, Shatin, NT, Hong Kong

[88]*INAF, Osservatorio Astronomico di Padova, Vicolo dell'Osservatorio 5, I-35122 Padova, Italy*
[89]*INFN, Trento Institute for Fundamental Physics and Applications, I-38123 Povo, Trento, Italy*
[90]*Università di Roma "La Sapienza," I-00185 Roma, Italy*
[91]*Université Libre de Bruxelles, Brussels 1050, Belgium*
[92]*Sonoma State University, Rohnert Park, California 94928, USA*
[93]*Montana State University, Bozeman, Montana 59717, USA*
[94]*Center for Interdisciplinary Exploration & Research in Astrophysics (CIERA), Northwestern University, Evanston, Illinois 60208, USA*
[95]*Cardiff University, Cardiff CF24 3AA, United Kingdom*
[96]*Universitat de les Illes Balears, IAC3—IEEC, E-07122 Palma de Mallorca, Spain*
[97]*The University of Texas Rio Grande Valley, Brownsville, Texas 78520, USA*
[98]*Bellevue College, Bellevue, Washington 98007, USA*
[99]*Institute for Plasma Research, Bhat, Gandhinagar 382428, India*
[100]*The University of Sheffield, Sheffield S10 2TN, United Kingdom*
[101]*University of Southern California Information Sciences Institute, Marina Del Rey, California 90292, USA*
[102]*California State University, Los Angeles, 5151 State University Dr, Los Angeles, California 90032, USA*
[103]*Università di Trento, Dipartimento di Fisica, I-38123 Povo, Trento, Italy*
[104]*Montclair State University, Montclair, New Jersey 07043, USA*
[105]*National Astronomical Observatory of Japan, 2-21-1 Osawa, Mitaka, Tokyo 181-8588, Japan*
[106]*Whitman College, 345 Boyer Avenue, Walla Walla, Washington 99362 USA*
[107]*School of Mathematics, University of Edinburgh, Edinburgh EH9 3FD, United Kingdom*
[108]*University and Institute of Advanced Research, Gandhinagar Gujarat 382007, India*
[109]*IISER-TVM, CET Campus, Trivandrum Kerala 695016, India*
[110]*University of Szeged, Dóm tér 9, Szeged 6720, Hungary*
[111]*Tata Institute of Fundamental Research, Mumbai 400005, India*
[112]*INAF, Osservatorio Astronomico di Capodimonte, I-80131 Napoli, Italy*
[113]*University of Michigan, Ann Arbor, Michigan 48109, USA*
[114]*American University, Washington, D.C. 20016, USA*
[115]*Rochester Institute of Technology, Rochester, New York 14623, USA*
[116]*University of Biał ystok, 15-424 Biał ystok, Poland*
[117]*SUPA, University of Strathclyde, Glasgow G1 1XQ, United Kingdom*
[118]*University of Southampton, Southampton SO17 1BJ, United Kingdom*
[119]*University of Washington Bothell, 18115 Campus Way NE, Bothell, Washington 98011, USA*
[120]*Institute of Applied Physics, Nizhny Novgorod 603950, Russia*
[121]*Seoul National University, Seoul 08826, Korea*
[122]*Inje University Gimhae, South Gyeongsang 50834, Korea*
[123]*National Institute for Mathematical Sciences, Daejeon 34047, Korea*
[124]*NCBJ, 05-400 Świerk-Otwock, Poland*
[125]*Institute of Mathematics, Polish Academy of Sciences, 00656 Warsaw, Poland*
[126]*OzGrav, School of Physics & Astronomy, Monash University, Clayton 3800, Victoria, Australia*
[127]*Hanyang University, Seoul 04763, Korea*
[128]*NASA Marshall Space Flight Center, Huntsville, Alabaman 35811, USA*
[129]*ESPCI, CNRS, F-75005 Paris, France*
[130]*Southern University and A&M College, Baton Rouge, Louisiana 70813, USA*
[131]*OzGrav, University of Melbourne, Parkville, Victoria 3010, Australia*
[132]*College of William and Mary, Williamsburg, Virginia 23187, USA*
[133]*Indian Institute of Technology Madras, Chennai 600036, India*
[134]*IISER-Kolkata, Mohanpur, West Bengal 741252, India*
[135]*Scuola Normale Superiore, Piazza dei Cavalieri 7, I-56126 Pisa, Italy*
[136]*Université de Lyon, F-69361 Lyon, France*
[137]*Hobart and William Smith Colleges, Geneva, New York 14456, USA*
[138]*Janusz Gil Institute of Astronomy, University of Zielona Góra, 65-265 Zielona Góra, Poland*
[139]*University of Washington, Seattle, Washington 98195, USA*
[140]*King's College London, University of London, London WC2R 2LS, United Kingdom*
[141]*Indian Institute of Technology, Gandhinagar Ahmedabad Gujarat 382424, India*

[142]*International Institute of Physics, Universidade Federal do Rio Grande do Norte, Natal RN 59078-970, Brazil*
[143]*Andrews University, Berrien Springs, Michigan 49104, USA*
[144]*Università di Siena, I-53100 Siena, Italy*
[145]*Trinity University, San Antonio, Texas 78212, USA*
[146]*Abilene Christian University, Abilene, Texas 79699, USA*

[†]Deceased.